

Deep Extragalactic Visible Legacy Survey (DEVILS): Consistent Multi-wavelength Photometry for the DEVILS Regions (COSMOS, XMM-LSS & ECDFS)

L. J. M. Davies^{1*}, J. E. Thorne¹, A. S. G. Robotham^{1,2}, S. Bellstedt¹, S. P. Driver¹, N. J. Adams³, M. Bilicki⁴, R. A. A. Bowler³, M. Bravo¹, L. Cortese^{1,2}, C. Foster^{2,5}, M. W. Grootes⁶, B. Häußler⁷, A. Hashemizadeh¹, B. W. Holwerda⁸, P. Hurley⁹, M. J. Jarvis^{3,10}, C. Lidman^{11,12}, N. Maddox¹³, M. Meyer^{1,2}, M. Paolillo^{14,15,16}, S. Phillipps¹⁷, M. Radovich¹⁸, M. Siudek^{19,20}, M. Vaccari^{10,21}, R. A. Windhorst²²

¹ ICRAR, The University of Western Australia, 35 Stirling Highway, Crawley, WA 6009, Australia

² ARC Centre of Excellence for All Sky Astrophysics in 3 Dimensions (ASTRO 3D)

³ Sub-department of Astrophysics, University of Oxford, Denys Wilkinson Building, Keble Road, Oxford OX13RH, UK

⁴ Center for Theoretical Physics, Polish Academy of Sciences, al. Lotników 32/46, 02-668 Warsaw, Poland

⁵ Sydney Institute for Astronomy, School of Physics, A28, The University of Sydney, NSW, 2006, Australia

⁶ Netherlands eScience Center, Science Park 140, 1098 XG Amsterdam, The Netherlands

⁷ European Southern Observatory, Alonso de Cordova 3107, Vitacura, Santiago, Chile

⁸ Department of Physics and Astronomy, 102 Natural Science Building, University of Louisville, Louisville KY 40292, USA

⁹ Astronomy Centre, Department of Physics & Astronomy, University of Sussex, Brighton, BN1 9QH, UK

¹⁰ Department of Physics and Astronomy, University of the Western Cape, Robert Sobukwe Road, Bellville 7535, South Africa

¹¹ Research School of Astronomy and Astrophysics, The Australian National University, ACT 2601, Australia

¹² Centre for Gravitational Astrophysics, College of Science, The Australian National University, ACT 2601, Australia

¹³ Faculty of Physics, Ludwig-Maximilians-Universität, Scheinerstr. 1, 81679 Munich, Germany

¹⁴ INAF - Osservatorio Astronomico di Capodimonte, Salita Moiariello 16, I-80131, Napoli, Italy

¹⁵ Dipartimento di Fisica, Università di Napoli "Federico II," via Cinthia 9, I-80126 Napoli, Italy

¹⁶ INFN - Sezione di Napoli, via Cinthia 9, I-80126 Napoli, Italy

¹⁷ H. H. Wills Physics Laboratory, University of Bristol, Tyndall Avenue, Bristol, BS8 1TL, UK

¹⁸ INAF - Osservatorio Astronomico di Padova, vicolo dell'Osservatorio 5, I-35122 Padova, Italy

¹⁹ Institut de Física d'Altes Energies (IFAE), The Barcelona Institute of Science and Technology, 08193 Bellaterra (Barcelona), Spain

²⁰ National Centre for Nuclear Research, ul. Pasteura 7, 02-093, Warsaw, Poland

²¹ INAF - Istituto di Radioastronomia, via Gobetti 101, 40129 Bologna, Italy

²² School of Earth & Space Exploration, Arizona State University, P.O. Box 871404, Tempe, AZ 85287-1404, USA

Accepted XXX. Received YYY; in original form ZZZ

ABSTRACT

The Deep Extragalactic Visible Legacy Survey (DEVILS) is an ongoing high-completeness, deep spectroscopic survey of $\sim 60,000$ galaxies to $Y < 21.2$ mag, over ~ 6 deg² in three well-studied deep extragalactic fields: D10 (COSMOS), D02 (XMM-LSS) and D03 (ECDFS). Numerous DEVILS projects all require consistent, uniformly-derived and state-of-the-art photometric data with which to measure galaxy properties. Existing photometric catalogues in these regions either use varied photometric measurement techniques for different facilities/wavelengths leading to inconsistencies, older imaging data and/or rely on source detection and photometry techniques with known problems. Here we use the ProFOUND image analysis package and state-of-the-art imaging datasets (including Subaru-HSC, VST-VOICE, VISTA-VIDEO and UltraVISTA-DR4) to derive matched-source photometry in 22 bands from the FUV to 500 μ m. This photometry is found to be consistent, or better, in colour-analysis to previous approaches using fixed-size apertures (which are specifically tuned to derive colours), but produces superior total source photometry, essential for the derivation of stellar masses, star-formation rates, star-formation histories, etc. Our photometric catalogue is described in detail and, after internal DEVILS team projects, will be publicly released for use by the broader scientific community.

Key words: methods: observational - techniques: photometric - catalogues - surveys - galaxies: general - galaxies: evolution

* E-mail: luke.j.davies@uwa.edu.au

1 INTRODUCTION

The advent of large area, high-completeness, spectroscopic surveys of the local Universe, coupled with deep panchromatic multi-wavelength imaging, and resulting robustly derived galaxy and environmental properties, have been revolutionary over the past two decades. Surveys such as the Sloan Digital Sky Survey (SDSS, York et al. 2000; Abazajian et al. 2009) and the Galaxy and Mass Assembly (GAMA, Driver et al. 2011; Hopkins et al. 2013; Liske et al. 2015; Driver et al. 2016a; Baldry et al. 2018) have compiled extensive databases of galaxy locations, distances, environments and physical properties leading to a complete and comprehensive analysis of ‘typical’ galaxies (*i.e.* $\geq 0.1 M^*$, one tenth the characteristic mass in the stellar mass function, and above) in the relatively local Universe. These surveys have fundamentally changed our understanding of the distribution of stellar mass (*e.g.* Baldry et al. 2012; Wright et al. 2017), star-formation (*e.g.* Kauffmann et al. 2003; Brinchmann et al. 2004; Davies et al. 2016b, 2017, 2019b), gas and stellar phase metallicity (*e.g.* Tremonti et al. 2004; Lara-López et al. 2013; Bellstedt et al. 2021), large-scale structure and group environments (*e.g.* Tegmark et al. 2004; Yang et al. 2007; Robotham et al. 2011; Blake et al. 2013; Alpaslan et al. 2014), pairs of galaxies (*e.g.* Patton et al. 2013; Robotham et al. 2014) and the impact of these environments on galaxy properties (*e.g.* Blanton et al. 2005; Ellison et al. 2008; Peng et al. 2010; Patton et al. 2011; Robotham et al. 2013; Alpaslan et al. 2016; Davies et al. 2015b, 2016a, 2019a).

However, this approach of successfully combining extensive panchromatic multi-wavelength imaging with high completeness spectroscopy to consistently measure galaxy and environmental properties has largely been limited to the relatively local Universe. While this can tell us a wealth of information regarding the end-point of the galaxy evolution process to date, it tells us little about the astrophysical process occurring over the preceding billions of years of Universal evolution. While numerous surveys have aimed at probing the evolution of galaxies outside of the local Universe ($z > 0.3$), they can not be well-matched to the local studies of SDSS and GAMA due to sometimes complex selection functions, incompleteness and/or varying analysis techniques. Until recently, the state of the art survey which probed this epoch (zCOSMOS-bright, Lilly et al. 2007) was encumbered by its very small area ($\sim 1 \text{ deg}^2$), sparse sampling, and complex footprint (due to slit-mask spectroscopy). This ultimately leads to low completeness (only $\sim 50\%$ to $i < 22$, see Davies et al. 2015). Other surveys at this epoch have focused on the sparse sampling of colour-selected populations over large volumes, such as the VIMOS Public Extragalactic Redshift Survey (VIPERS, Guzzo et al. 2014; Scodreggio et al. 2018) and DEEP2/3 (Cooper et al. 2012; Newman et al. 2013). The designs of these surveys, while matched to their specific science goals, are not tuned to provide a comparable sample to more local studies and are inadequate for studying the evolution of galaxy groups, mergers, sub-Mpc structure and the influence of environment on galaxy evolution – a key requirement in understanding the evolutionary processes which are shaping galaxies.

The new Deep Extragalactic Visible Legacy Survey (DEVILS, Davies et al. 2018) is a high completeness, deep spectroscopic survey aimed at providing a direct counterpart to GAMA but at a much earlier epoch ($0.3 < z < 1$). Unlike previous samples DEVILS does not apply any colour selection, does not sparsely sample the population (*i.e.* is flux-limited only), and will use identical source selection and analysis techniques to samples in the local Universe. This will allow similar studies to GAMA and SDSS, but at a much earlier point in cosmic time. Importantly, within DEVILS we will apply identical data processing and analysis techniques to GAMA to minimise any

potential errors/inconsistencies in the approach applied, *i.e.* it is difficult to compare measurements from surveys at low and high redshift, which use different selection methods, approaches and measurement techniques leading to potential errors when probing galaxy evolution processes.

The foundation of many derived astrophysical properties of galaxies are robust observed images/photometric measurements coupled with redshifts. With just these data products in hand, an extensive array of measurements can be made, such as stellar masses (Kauffmann et al. 2003; Baldry et al. 2010; Taylor et al. 2015), star-formation rates (Brinchmann et al. 2004; Davies et al. 2016b) and star-formation histories (*e.g.* Kauffmann et al. 2003; Bellstedt et al. 2020, Thorne et al. 2021), metallicities (*e.g.* Tremonti et al. 2004; Bellstedt et al. 2021, Thorne et al. in prep.), morphological classifications (*e.g.* Moffett et al. 2016; Hashemizadeh et al. 2021) and structural component analyses (*e.g.* Lange et al. 2015). The DEVILS spectroscopic observations are currently being undertaken at the Anglo-Australian Telescope (AAT) (see Davies et al. 2018, and below). However, the next stage of producing these derived properties for our sample is to acquire robust photometric measurements of galaxies in the DEVILS regions.

Importantly for direct comparisons to $z \sim 0$, this photometry must be derived using an almost identical method to that used in GAMA. Recently, Bellstedt et al. (2020), produced new multi-wavelength photometric measurements for the GAMA sample using the PROFOUND (Robotham et al. 2018) source detection and photometry code. In this work we apply the same process (albeit with small changes where appropriate) to the deep photometric data available in the DEVILS regions. While there are existing photometric catalogues in these fields (most notably in the COSMOS region from COSMOS2015 and G10/COSMOS, Laigle et al. 2016; Andrews et al. 2017), these catalogues typically used imaging data that has since been superseded by more recent higher quality data, and disparate measurement techniques at different wavelengths, which are then matched together in catalogue space. In addition, these samples were compiled with pre-Gaia astrometry, which can now be improved upon using the updated astrometric accuracy Gaia provides. This can lead to inconsistencies/errors from *e.g.* errors in position matching and/or blending of sources. In addition, no consistent photometry currently exists across all of the DEVILS regions (COSMOS, XMM-LSS, ECDFS). With this in mind, in this work we derive new photometric measurements in the DEVILS regions using the most up-to-date imaging available, in a consistent way from FUV to FIR wavelengths and in a largely identical manner to GAMA to allow direct comparisons to $z \sim 0$.

This photometry is already being used in a number of projects within the DEVILS survey (*e.g.* Thorne et al. 2020; Hashemizadeh et al. 2021; Koushan et al. 2021, Thorne et al. in prep., Hashemizadeh et al. in prep.) and will form the basis for many subsequent studies. In this paper we fully document the source finding, photometric derivation, masking, star-galaxy separation and catalogue compilation of the photometry used in these science projects. Following this we also utilise our new photometry catalogues to produce and tabulate deep multi-wavelength number counts for broader use. Once our catalogues have been used for internal team projects, they will be made publicly available to the wider community via the DEVILS data release 1 (Davies et al. in prep.).

All magnitudes reported here are in the AB system and when necessary we assume a cosmology with $H_0 = 70 \text{ km s}^{-1} \text{ Mpc}^{-1}$, $\Omega_m = 0.3$, and $\Omega_\Lambda = 0.7$.

2 THE DEEP EXTRAGALACTIC VISIBLE LEGACY SURVEY

Briefly, DEVILS is an ongoing spectroscopic and multi-wavelength survey being undertaken with the Anglo-Australian Telescope (AAT). The survey aims to build a high completeness ($>85\%$) sample of $\sim 60,000$ galaxies to $Y < 21.2$ mag in three well-studied deep extragalactic fields: D10 (COSMOS), D02 (ECDFS) and D03 (XMM-LSS). This sample will provide the first high spectroscopic completeness flux-limited sample at intermediate redshifts, allowing for the robust parametrisation of group and pair environments in the distant Universe. In addition to the spectroscopic survey, the DEVILS team will also compile an extensive database of multi-wavelength-derived properties for sources in the DEVILS spectroscopic sample, such as spectral energy distribution (SED) fits, star-formation histories, stellar masses, star-formation rates and metallicities (see Thorne et al in prep.), and morphologies and structural parameters (see Hashemizadeh et al, in prep.) - with the work presented here forming the basis of this database. The spectroscopic component of the survey is currently $\sim 70\%$ complete, and is due to finish spectroscopic observations in late 2021. The science goals of the project are varied, from the environmental impact on galaxy evolution at intermediate redshift, to the evolution of the halo mass function over the last ~ 7 billion years. For full details of the survey science goals, survey design, target selection and spectroscopic observations see [Davies et al. \(2018\)](#). In this paper we describe our new multi-wavelength photometric catalogue, which will be used in the core DEVILS science projects.

2.1 The DEVILS Regions

The DEVILS regions were specifically selected to cover areas with extensive existing and upcoming imaging campaigns to facilitate broad range of science topics.

The D10 field represents a sub-region of the Cosmic Evolution Survey field (COSMOS, [Scoville et al. 2007](#)), covering 1.5 deg^2 of the UltraVISTA ([McCracken et al. 2012](#)) region and centred at $R.A.=150.04^\circ$, $Dec=2.22^\circ$. This region is covered by an extensive array of imaging and spectroscopic data ranging from x-ray to low-frequency radio continuum observations (see Table 1 for data in the FUV-FIR regime). The DEVILS spectroscopic target catalogue in this region is selected from the UltraVISTA DR4 Y-band observations and includes all extragalactic sources to $Y < 21.2$ mag (see [Davies et al. 2018](#)). We do not discuss in detail the DEVILS spectroscopic campaign further in this work.

The D02 region covers the central 3 deg^2 of the XMM Large-Scale-Structure field (XMM-LSS) centred at $R.A.=35.53^\circ$, $Dec=-4.70^\circ$. This region is also covered by extensive imaging data, which is largely consistent in facility/filter coverage to D10. The main and important difference to the imaging data in D10, is that the NIR imaging comes from the Vista Deep Extragalactic Survey (VIDEO, [Jarvis et al. 2013](#)), which is consistent in facility/filters to UltraVISTA but shallower in depth (see Table 1).

Finally, the D03 region covers the central 1.5 deg^2 of the Extended Chandra Deep Field South (ECDFS) centred at $R.A.=53.15^\circ$, $Dec=-28.0^\circ$. This region contains similar photometric datasets to D02 in the UV and NIR-FIR, but differs in the optical (described below and see Table 1). The DEVILS spectroscopic target catalogues in D02 and D03 are selected from the VIDEO Y-band and also includes all extragalactic sources to $Y < 21.2$ mag (see [Davies et al. 2018](#)).

3 IMAGING DATASETS

In this section, we briefly describe the various imaging datasets in each of the DEVILS regions, and the surveys in which they were undertaken. The coverage of these data in each of these fields are displayed in Figures 2, 3, 4 and a summary of all data is given in Table 1. In order to display the depth of the various imaging datasets in comparison to the typical galaxies we will parameterise with DEVILS, Figure 1 shows the point source depth of the D10 imaging in-comparison to the spectral energy distribution of a typical galaxy within the DEVILS spectroscopic sample (note D02/D03 are roughly comparable in depth, but see Table 1 for differences). In the following subsections, unless otherwise stated, when combining data using SWARP ([Bertin et al. 2002](#)) we use the following settings: i) we set the centre of each field to the centre of the respective DEVILS region, ii) we set the pixel scale to that of the VISTA imaging used in our detection image (see Section 5.2 for more details), iii) we set the image size to cover the full DEVILS region $\pm 0.05 \text{ deg}$ buffer, iv) we do not use a weight map or mask in the combination, v) we apply a median combining process where frames overlap in sky position (this is only true for the GALEX and CFHT - u data in D02 and D03, all other data does not require combination), and vi) we do not apply a background subtraction at the SWARP combination stage as ProFOUND performs its own background subtraction when extracting photometric measurements.

3.1 Ultraviolet

3.1.1 GALEX (D10/D02/D03)

The COSMOS region was observed using the Galaxy Evolution Explorer (GALEX) space telescope as part of the Deep Imaging Survey ([Zamojski et al. 2007](#)). The telescope was equipped with a 0.5 m mirror, a circular field of view with 1.2 deg diameter, a $1.5''$ pixel^{-1} detector and two passbands in the far and near-ultraviolet (FUV and NUV, respectively). Observations in the D10/COSMOS region consisted of four pointings in each band with exposure times of $45,000 \text{ s}$ in FUV with a point spread function (PSF) full width at half-maximum (FWHM) of $5.4''$, and $50,000 \text{ s}$ in NUV with a PSF FWHM of $5.6''$. This data reaches a 5σ point source limiting depth of 26.0 and 25.6 mag (AB) in the FUV and NUV channels, respectively (see Table 1 and Figure 1). In this work we combine the four GALEX pointings in each band into a single mosaic covering the full D10 region using SWARP. In this process background subtraction is turned off due to the low photon statistics in the GALEX imaging resulting in poor background subtraction (see top left panels of Figure 2).

D02 and D03 have also been observed using the Galaxy Evolution Explorer (GALEX) space telescope as part of various imaging programs undertaken by different survey teams. To maximise the depth and coverage of the data available, we identify all GALEX pointings in the MAST database that overlap with the D02 and D03 spectroscopic regions. The images are then combined using SWARP, with background subtraction turned off (see top left panels of Figure 3 and 4). While this process results in slightly varying depth across the image, our resultant photometry uses a local sky background estimate to determine photometric errors, and thus takes the varying depth into account. For reference, the 5σ point-source depth is measured to vary from $\sim 23.5 - 25.5 \text{ mag}$ across the region.

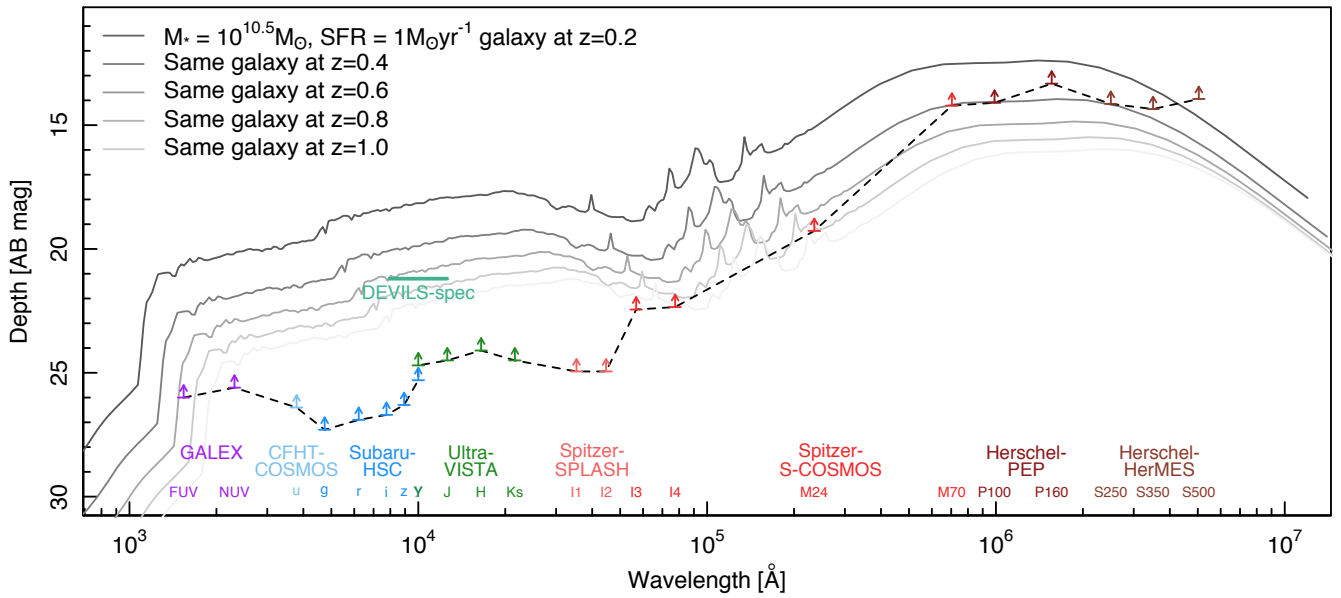


Figure 1. The survey-quoted nominal 5σ point source photometric depth of multi-wavelength data in the D10 region displaying an example of the typical depth of data covering the DEVILS regions (arrows joined by dashed line). The grey curves show a $M_*=10^{10.5} M_\odot$ and $SFR=1 M_\odot \text{ yr}^{-1}$ galaxy at $z=0.2, 0.4, 0.6, 0.8$ and 1.0 , generated using ProSPECT. The depth of imaging in the D10 region means that a typical galaxy will be detected in *GALEX*-NUV to *Spitzer*-IRAC out to $z \sim 1$. The imaging data extends to much greater depth than the DEVILS spectroscopic campaign.

3.2 Optical

3.2.1 CFHT - *u* (D10/D02)

The *u*-band images in D10 and D02 were obtained as part of the Canada-France-Hawaii Telescope Legacy Survey (CFHT-LS¹). In D10, the CFHT-LS deep survey covers the central 1 deg^2 of the field, but is also supplemented by independent CFHT observations outlined in Capak et al. (2007) to cover the full 1.5 deg^2 . To maximise the depth of these data and to have coverage over the full D10 region, we combine the CFHT-LS and Capak et al. (2007) data into a single image using SWARP. Both data sets were obtained using Mega-Prime camera on CFHT with a 1 deg^2 field of view with a native resolution of $0.18'' \text{ pixel}^{-1}$. For CFHT-LS the worst case seeing was $0.9''$ and the 5σ point source limiting magnitude is 26.6 mag. For the Capak et al. (2007) data the worst case seeing was also $0.9''$ and the 5σ point source limiting magnitude is 26.4 mag. The D02 region is covered by a combination of the CFHT-LS deep 1 region (D1, 5σ point source depth ~ 26.25 mag) and wide 1 region (W1, 5σ point source depth ~ 25.3 mag). To maximise the depth and coverage, we obtain all D1 and W1 data from the CFHT archive and combine using SWARP.

3.2.2 Subaru-HSC - *g,r,i,z* (D10/D02)

For our optical, *griz*, imaging in the D10 and D02 region we use the new second public data release (PDR2 Aihara et al. 2019) of the Subaru Telescope's Hyper Suprime-Cam Subaru Strategic Program (HSC-SSP, see Aihara et al. 2018a,b). HSC is an optical imaging camera on the 8.2m mirror Subaru Telescope, covering a 1.5 deg diameter field of view to $0.168'' \text{ pixel}^{-1}$ resolution. As part of the Deep+Ultra-Deep (DUD) SSP program, the HSC team have released 31 deg^2 of

DUD imaging including the extended-COSMOS and XMM-LSS regions. Data reaches a 5σ point source limiting magnitude of 27.3, 26.9, 26.7, 26.3, 25.3 mag in *grizy*, respectively (quoted by the HSC-SSP team). To obtain these data, we independently download overlapping $0.25 \times 0.25 \text{ deg}$ regions in all bands from the HSC data access cutout server² and combined using SWARP.

3.2.3 VST-VOICE - *u,g,r,i* (D03)

Both CFHT-LS and HSC-SSP programs do not cover the D03 region due to its southern nature. As such, for our optical, *ugri* imaging we use the first data release of the VST Optical Imaging of the CDFS and ES1 Fields (VOICE, Vaccari et al. 2016) Survey. The VOICE data covers 4 deg^2 of the ECDFS region with four pointings reaching a 5σ point source limiting magnitude of 25.3, 26.4, 26.1, 25.2 mag in *ugri*, respectively. The survey is undertaken on the 2.6m VLT Survey Telescope (VST) using OmegaCAM with a $0.21''/\text{pixel}$ resolution. In addition, the *ugri* imaging is also supplemented by partial coverage of the field in the VIDEO Z-band (see below).

3.3 Near Infrared

3.3.1 UltraVISTA-DR4 (D10)

The near-IR UltraVISTA survey (McCracken et al. 2012) is a recently completed survey on the Visible and Infrared Survey Telescope for Astronomy (VISTA) using the VISTA Infrared Camera (VIRCAM). VIRCAM covers a 1.65 deg diameter field of view with $0.34'' \text{ pixel}^{-1}$ native resolution. The UltraVISTA team observe a single pointing centred on the COSMOS region, and are resampled to a $0.15'' \text{ pixel}^{-1}$ resolution. Here we use the fourth UltraVISTA public data

¹ <http://www.cfht.hawaii.edu/Science/CFHLS/>

² https://hsc-release.mtk.nao.ac.jp/das_cutout/pdr2/

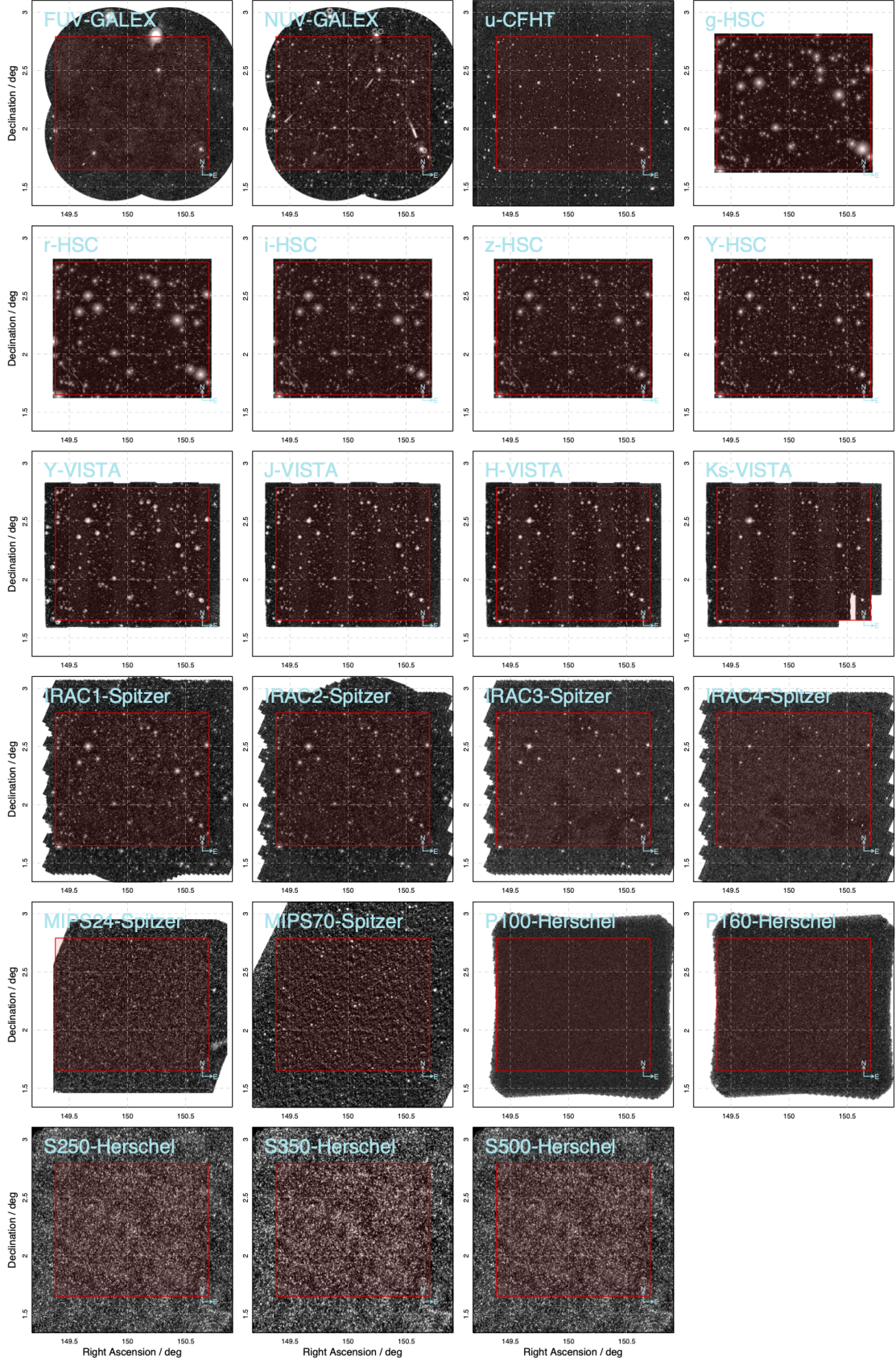


Figure 2. Multi-wavelength data covering the D10 region. The D10 spectroscopic region is displayed as the red box. Note that the HSC data are only downloaded to cover the D10 region (with a small buffer). The raw HSC data covers a larger area.

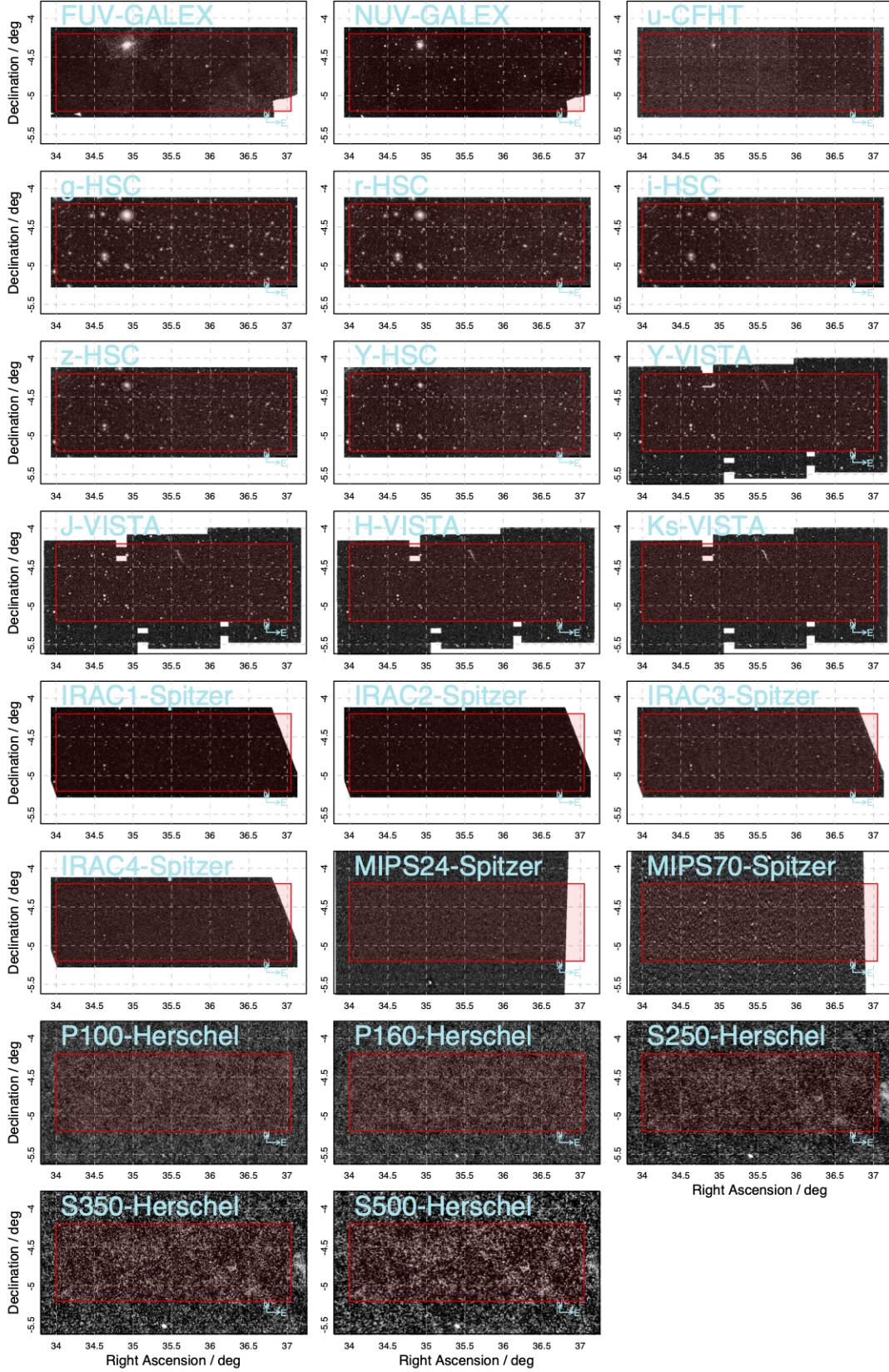


Figure 3. Multi-wavelength data covering the D02 region. The D02 spectroscopic region is displayed as the red box. Data from GALEX, CFHT, HSC and *Spitzer*-IRAC is combined using SWARP to only cover the D02 region, but the original data does extend to larger areas.

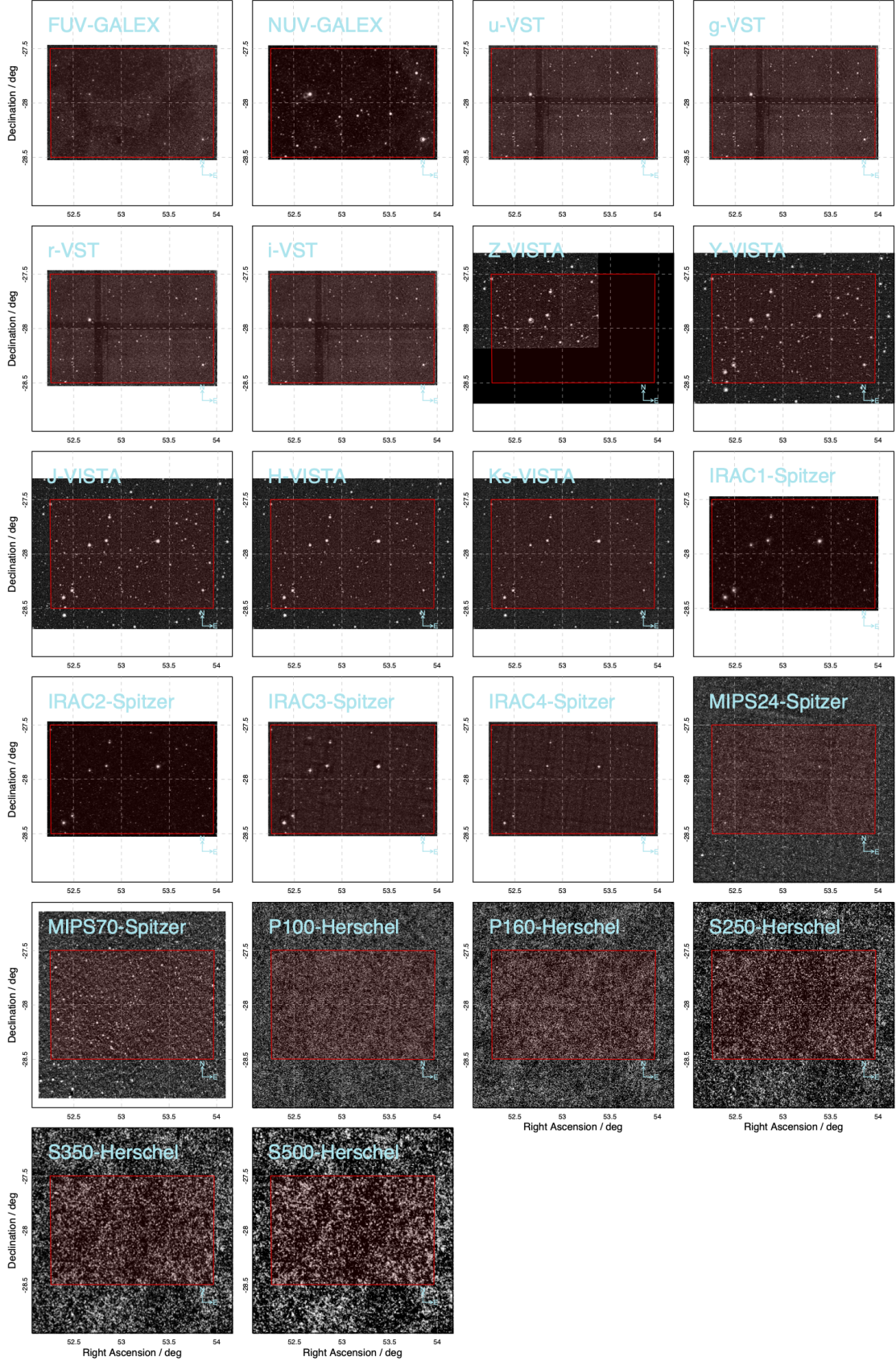


Figure 4. Multi-wavelength data covering the D03 region. The D03 spectroscopic region is displayed as the red box. Note that data from GALEX, VST and *Spitzer*-IRAC is combined using SWARP to only cover the D03 region. The original data does extend to larger areas. Note that Z-band VISTA data does not cover the full region, but is the only available deep Z-band imaging the D03 field.

release (DR4³), which comprises of stacked Y, J, H, Ks images using data taken between 2009 and 2016, with a total exposure time of >11 h in each band/pixel. Typical FWHM seeing of the stacked data is $\sim 0.75''$ and the 5σ point source limiting magnitudes are 24.7, 24.5, 24.1, 24.5 mag, in the deep regions and 25.8, 25.6, 25.2, 24.9 mag, in the ultra-deep region (see McCracken et al. 2012, for details) in Y, J, H and Ks respectively. Data are downloaded from the ESO public archive.

3.3.2 VIDEO (D02/D03)

Complementary to the UltraVISTA imaging in D10, the VISTA Deep Extragalactic Observations (VIDEO Jarvis et al. 2013) Survey has covered 12 deg^2 of three deep extragalactic fields using VISTA-VIRCAM in Z, Y, J, H and Ks bands - completely covering the D02 and D03 regions in YJHKs. Unlike UltraVISTA, VIDEO data are resampled to a $0.2'' \text{ pixel}^{-1}$ resolution. For our catalogues we use the VIDEO team-internal 2019-11-08 stacked images, reaching full survey depth. Data with $> 0.9''$ seeing are rejected from these stacks and final 5σ point source limiting magnitudes are 25.7, 24.6, 24.5, 24.0 and 23.5 mag in Z, Y, J, H and Ks respectively. In D02 we use only YJHKs for our imaging catalogues and opt to use the HSC z-band data to be consistent with D10. However, as noted above, in D03 we do not have HSC coverage and therefore use the VIDEO Z-band data, which due to an updated strategy implemented during the VIDEO survey is incomplete and shallower (see Figure 4). For details of the VIDEO survey and data, see Jarvis et al. (2013).

3.4 Mid Infrared

3.4.1 S-COSMOS and Spitzer-SPLASH (D10)

The COSMOS *Spitzer* survey (S-COSMOS, Sanders et al. 2007), is a 3-160 μm survey of the COSMOS region using all seven bands of the *Spitzer* Infrared Array Camera (IRAC) and the Multiband Imaging Photometer for *Spitzer* (MIPS) instruments. The IRAC instrument covers four NIR-MIR filters centred at 3.6, 4.5, 5.6, 8.0 μm over a 27 arcmin^2 field of view with native $1.2'' \text{ pixel}^{-1}$ resolution. MIPS covers three MIR-FIR filters centred at 24, 70 and 160 μm with native resolution of 1.2, 4.0 and $8.0'' \text{ pixel}^{-1}$ respectively.

Following the S-COSMOS campaign, and during *Spitzer's* 'warm' mission phase once the cryogenics had been exhausted, the COSMOS field was observed by the *Spitzer* Large Area Survey with Hyper-Suprime-Cam (SPLASH) survey at 3.6 and 4.5 μm increasing the depth and area coverage in these bands (see Lin et al. 2016; Laigle et al. 2016). Both SPLASH and S-COSMOS IRAC data have been resampled to $0.6'' \text{ pixel}^{-1}$ resolution by their respective teams, with typical PSF FWHM of 1.7, 1.7, 1.9 and $2.0''$ for the IRAC bands respectively.

Here we use the superior SPLASH IRAC 3.6 and 4.5 μm data reaching a 5σ point source limiting magnitude of 24.9 in both bands, and S-COSMOS IRAC 5.6 and 8.0 μm , and MIPS 24 and 70 μm reaching a 5σ point source limiting magnitude of 22.4, 22.3, 19.3, and 14.2 mag respectively. We do not use the MIPS 160 μm data in favour of the deeper *Herschel* data that exist in this region (see below).

3.4.2 SERVS and SWIRE (D02/D03)

Both D02 and D03 are covered by the *Spitzer* Extragalactic Representative Volume Survey (SERVS, Mauduit et al. 2012) survey at 3.6 and 4.5 μm (IRAC1 and IRAC2). SERVS is an 18 deg^2 medium-deep survey with the post-cryogenic *Spitzer* Space Telescope reaching $\sim 2 \text{ mJy}$ ($\text{AB}=23.1 \text{ mag}$) depth of five deep astronomical fields (ELAIS-N1, ELAIS-S1, Lockman, ECDFS and XMMLSS). We use the DR1 release of the SERVS data products which reach a 5σ point source limiting magnitudes of 22.48 and 22.07 in S36 and S45, respectively.

At longer wavelengths, both fields are covered by the *Spitzer* Wide-area InfraRed Extragalactic (SWIRE, Lonsdale et al. 2003) survey at 3.6, 4.5, 5.8, 8.0, 24, 70 and 160 μm (IRAC1234, MIPS123). SWIRE has surveyed $\sim 50 \text{ deg}^2$ centred on the same deep fields as SERVS, but to a shallower depth. Here we use the DR5 SWIRE images at 5.8, 8.0, 24 and 70 μm , opting to use the deeper SERVS data for IRAC 1 and 2 and *Herschel* data for 160 μm . The DR5 data reaches 5σ point source limiting magnitudes of 19.7, 19.96, 18.0 at 13.26 mag at 5.8, 8.0, 24 and 70 μm , respectively. Both SERVS and SWIRE data are obtained from the NASA/IPAC Infrared science archive⁴.

3.5 Far Infrared

3.5.1 Herschel-PACS Evolutionary Probe (D10)

The PACS (Photodetector Array Camera and Spectrometer) Evolutionary Probe (PEP, Lutz et al. 2011) was a *Herschel* key program covering a number of deep fields at 100 and 160 μm , including COSMOS. The PACS instrument has a field of view of $1.75 \times 3.5 \text{ arcmin}$, and 1.2 and $2.4'' \text{ pixel}^{-1}$ resolution at 100 and 160 μm , respectively.

In this paper we use the first PEP data release⁵ which imaged the COSMOS region reaching a 5σ point source limiting magnitude of 14.1 and 13.3 mag at 100 and 160 μm , with a PSF FWHM of 7.4 and $11.3''$, respectively.

3.5.2 Herschel-HerMES (D10/D02/D03)

The *Herschel* Multi-Tiered Extragalactic Survey (HerMES, Oliver et al. 2012) is a far-IR survey conducted using *Herschel's* Spectral and Photometric Imaging Receiver (SPIRE). As part of HerMES, the COSMOS region was observed at 250, 350 and 500 μm with a pixel scale 6.0, 8.3 and $12.0'' \text{ pixel}^{-1}$ and FWHM of 18.15, 25.15 and $36.3''$, respectively. The XMMLSS and ECDFS regions were also observed by HerMES and cover both PACS 100 and 160 μm and SPIRE 250, 350 and 500 μm .

In this work we use the second HerMES data release⁶ which reaches 5σ point source limiting magnitudes of 12.4, 11.6, 14.1, 14.4 mag and 13.9 at 100, 160, 250, 350 and 500 μm , respectively. Construction of the HerMES images is described in detail in Levenson et al. (2010) and Viero et al. (2013).

Note, for the rest of this paper we will predominantly only show figures and quote numbers for the D10 region. The reason for this is two-fold, firstly the D10 region has superior existing photometric catalogues with which to compare to, and secondly, for ease of description. However, we note that our process is identical in the D02/D03 regions.

⁴ <https://irsa.ipac.caltech.edu/frontpage/>

⁵ <http://www.mpe.mpg.de/ir/Research/PEP/DR1>

⁶ <http://hedam.lam.fr/HerMES/>

³ <http://ultravista.org/release4/>

Table 1. Overview of multi-wavelength data in the DEVILS regions used in this photometric analysis. For further details see sections 3. Nominal Depth is the depth quoted by the respective survey, while Measured Depth is the depth to galaxy sources derived from the turn-over point in the galaxy number counts (see Section 8) For the common data in D02 and D03 the Measured Depth column displays D02 " / " D03 depths.

Field	Common Name(s)	Facility	Survey	Band	Central Wavelength (μm)	Nominal Depth (5σ AB)	Measured Depth (AB)	Zero-point (AB)	Ref
D10	COSMOS	GALEX	GALEX-DIS	FUV	0.154	26.0	28.42	18.82	Zamojski et al. (2007)
				NUV	0.231	25.6	27.37	20.08	— —
		CFHT	CFHT-COSMOS	u	0.379	>26.4	26.36	30.00	Capak et al. (2007)
				g	0.474	27.3	26.09	27.80	Aihara et al. (2019)
		Subaru	HSC-SSP (DUD)	r	0.622	26.9	25.82	27.70	— —
				i	0.776	26.7	25.09	27.60	— —
				z	0.893	26.3	25.41	27.80	— —
				y	1.00	25.3	24.90	26.20	— —
				Y	1.02	>24.7	25.46	30.00	McCracken et al. (2012)
				J	1.26	>24.5	25.22	30.00	— —
				H	1.65	>24.1	24.98	30.00	— —
				Ks	2.16	>24.5	24.75	30.00	— —
		Spitzer	SPLASH	S36	3.53	24.9	24.66	21.58	Laigle et al. (2016)
				S45	4.47	24.9	24.77	21.58	— —
			S-COSMOS	S58	5.68	22.4	23.86	21.58	Sanders et al. (2007)
				S80	7.75	22.3	23.90	21.58	— —
		<i>Herschel</i>	PEP	MIPS24	23.5	19.3	18.53	20.15	— —
				MIPS70	70.4	14.2	-	17.53	— —
			PEP	P100	98.9	14.1	14.93	8.90	Lutz et al. (2011)
			PEP	P160	156	13.3	14.07	8.90	— —
			HerMES	S250	250	14.1	14.24	11.44 [†]	Oliver et al. (2012)
			HerMES	S350	350	14.4	14.30	11.43 [†]	— —
			HerMES	S500	504	13.9	14.64	11.44 [†]	— —
D02 & D03	XMMLSS & ECDFS	GALEX	multiple	FUV	0.154	~25.0	27.32/27.04	18.82	multiple
				NUV	0.231	~25.0	26.70/27.02	20.08	— —
		VISTA	VIDEO	Y	1.02	24.6	24.65/24.82	30.00	Jarvis et al. (2013)
				J	1.26	24.5	24.34/24.45	30.00	— —
				H	1.65	24.0	24.05/24.14	30.00	— —
				Ks	2.16	23.5	23.84/23.9	30.00	— —
		Spitzer	SERVS	S36	3.53	22.48	23.45/23.97	21.58	Mauduit et al. (2012)
				S45	4.47	22.07	23.08/23.98	21.58	— —
			SWIRE	S58	5.68	19.70	22.31/22.64	21.58	Lonsdale et al. (2003)
				S80	7.75	19.96	22.33/22.70	21.58	— —
		<i>Herschel</i>	HerMES	MIPS24	23.5	18.00	18.26/18.21	20.15	— —
				MIPS70	70.4	13.26	-/-	17.53	— —
				P100	98.9	12.4	13.77/13.67	8.90	Oliver et al. (2012)
				P160	156	11.6	13.07/12.98	8.90	— —
				S250	250	14.1	13.99/13.99	11.44 [†]	— —
				S350	350	14.4	14.03/14.07	11.43 [†]	— —
				S500	504	13.9	14.27/14.29	11.44 [†]	— —
D02	XMMLSS	CFHT	CFHT-LS	u	0.379	>25.3	25.68	30.00	CFHTLS
				g	0.474	27.3	25.50	27.80	Aihara et al. (2019)
		Subaru	HSC-SSP (DUD)	r	0.622	26.9	25.19	27.70	— —
				i	0.776	26.7	24.94	27.60	— —
				z	0.893	26.3	24.75	27.80	— —
				y	1.00	25.3	23.97	26.20	— —
D03	ECDFS	VST	VOICE	u	0.379	25.3	25.76	30.00	Vaccari et al. (2016)
				g	0.474	26.4	25.58	30.00	— —
				r	0.622	26.1	25.33	30.00	— —
				i	0.776	25.2	24.89	30.00	— —
		VISTA	VIDEO	Z	0.893	25.7	25.65	30.00	Jarvis et al. (2013)

[†] SPIRE maps are in units of Jansky per Beam and to generate these zero-points we have added a factor $2.5 \log_{10}(B/N^2)$ where B is the beam size given as 373, 717, and 1494 sq " and N is the pixel size given as 6.0, 8.3 and 12 " in 250, 350 and 500 μm , respectively.

4 THE NEED FOR A NEW COSMOS (D10) PHOTOMETRIC CATALOGUE

There have been a number of multi-wavelength photometric catalogues produced in the COSMOS region over the past two decades, such as those outlined in Capak et al. (2007), Laigle et al. (2016) and for the central 1 deg^2 discussed in Andrews et al. (2017) and Driver et al. (2018). However, as noted in Section 1, these catalogues have relied on software that causes some known issues when deriving total photometry catalogues across a broad range of source types and sizes. They have relied on table-matching of photometry derived by different teams using varied techniques, and/or do not contain the most up-to-date imaging in the region (such as UltraVISTA DR4 and HSC). As such, we now derive a new photometry catalogue which uses a state-of-the-art photometry code, designed to overcome issues in current catalogues. This enables us to measure photometry consistently from the UV-FIR with a single package on homogenised data, and include the most up-to-date imaging campaigns in this region.

Through the process of producing the G10/COSMOS catalogue outlined in Andrews et al. (2017) and, using a similar method, the GAMA photometric catalogues (see Driver et al. 2016a; Wright et al. 2016), we identified a number of issues when determining total source photometry. Briefly, within both of these surveys initial source detection was undertaken using SOURCE EXTRACTOR (Bertin & Arnouts 1996) to define elliptical apertures. However, it was quickly identified that these apertures are prone to some issues, such as bright galaxy fragmentation into a number of sub-apertures, and highly erroneous apertures, largely due to the aperture following an isophotal bridge to loop around a nearby bright star (these issues mostly arise because of the difficulty in simultaneously measuring fluxes for both very bright and very faint sources). For details of these issues see Robotham et al. (2018) and Davies et al. (2018). These errant apertures led to a significant fraction ($\sim 10\%$) of sources having poorly measured photometry. To overcome these issues in the G10/COSMOS sample and in GAMA (see Andrews et al. 2017; Wright et al. 2016, respectively), we undertook a systematic, and time-consuming, visual inspection and manual fixing of the errant apertures both within the teams and via a citizen science project (AstroQuest⁷).

Motivated by the level of manual fixing required in the GAMA and G10/COSMOS data, we developed a new source finding and photometry code, ProFOUND (Robotham et al. 2018). Briefly, the ProFOUND code has three fundamental differences to its approach over SOURCE EXTRACTOR. Firstly, ProFOUND does not measure source photometry based on elliptical apertures, but identifies and retains the source isophote, allowing for both simple and irregular shapes (called segments). Secondly, these initial segments are dilated until the flux converges providing a pseudo-total flux. Thirdly, ProFOUND applies a watershed deblending approach where during the dilation, segments cannot overlap (*i.e.*, all the flux in any one pixel is allocated to one galaxy only). This is different to SOURCE EXTRACTOR, where hierarchical or nested-deblending allows for overlapping elliptical apertures and the possibility of flux being double counted. While the merits and failings of these approaches can be argued - through numerous tests we have found that the ProFOUND approach is far less likely to go catastrophically wrong and produces more robust photometric measurements. For full details on ProFOUND and numerous tests, we refer the reader to the code description paper Robotham et al. (2018) and four recent applications to the DEVILS input catalogue (Davies et al. 2018), GAMA photometry (Bellstedt et al. 2020), the

VISTA VIKING datasets (Koushan et al. 2021) and evolution of the high redshift stellar mass function (Adams et al. 2020).

In this work we apply the ProFOUND software to the state-of-the-art UV-FIR photometric data in the DEVILS regions. This is done in two modes, firstly using the vanilla ProFOUND multi-band approach to the UV-MIR data (described in Section 5), and secondly applying a new Bayesian technique to extract photometry in the unresolved MIR-FIR regime (described in Section 6). A similar approach has been applied in our shallower updated GAMA photometry, as outlined in Bellstedt et al. (2020). We note that we do not present new photometric measurements to the medium- and narrow-band Subaru Suprime-cam data in the D10 (COSMOS) region. This is largely due to the fact that we are aiming for consistent photometric catalogues across all of the DEVILS fields. As comparable data does not exist in the D02 and D03 regions, we do not include it here. We also note that in our SED fitting analysis of the D10 sample, presented in Thorne et al. (2020), we find little improvement/changes to measurements of stellar mass and star-formation rate when including the medium- and narrow-band data. Where this data is of significant benefit is in the derivation of photometric redshifts where finer wavelength sampling allows for greater redshift precision. However, we do not derive new photometric redshifts here as the COSMOS2015 sample already obtains robust photometric redshift measurements for these systems using the medium-band and narrow-band, and it is unlikely that we could significantly improve upon this.

5 UV-MIR PHOTOMETRIC MEASUREMENTS

5.1 ProFOUND Source Detection, Rebuilding Fragmented Galaxies and Splitting Merged Systems

To use ProFOUND to first identify target sources, we produce an inverse variance weighted stacked image from the UltraVISTA (D10) and VIDEO (D02/D03) Y, J, and H band images. Note that we do not use Ks because the UltraVISTA Ks image does not cover the same spatial extent as the other bands in D10 and has a small region of the DEVILS field missing. In D02/D03 we use the VIDEO Y, J, and H images only for consistency. This stacking allows us to maximise the depth in the initial detection image and remove any artefacts associated with a single band. This is a similar process to that outlined in Davies et al. (2018) for the DEVILS input catalogues. This stacking process is handled internally by ProFOUND using the PROFOUND-MULTIBAND command, allowing the user to specify one or more bands for source detection. If more than one band is supplied the images are inverse variance weighted stacked. We note here that one could opt to add additional bands in our stacking procedure (*i.e.* at bluer wavelengths) to both increase the source identification depth and potentially include bluer sources which are undetected in the NIR. However, we do not do this for a number of reasons: i) We wish to have a DEVILS survey selection band which is close to a single band measurement of stellar mass (*i.e.* $>4000\text{\AA}$ in the rest-frame) for all galaxies to $z \sim 1$. This necessitates the NIR bands. We use our stack for source detection and then Y-band magnitude to select our spectroscopic sample. As such, we would not target faint blue galaxies that are undetected in the Y-band. ii) The NIR data used here is already far deeper than that which we would use for science. So the faint blue sources that are undetected in the NIR are unlikely to be included in our science samples. This is especially true when performing a stellar mass-based selection (*i.e.* as in Thorne et al. 2020), and which will be done for all DEVILS core science, and iii) we wish to have consistency in the detection filters across all DEVILS

⁷ <https://astroquest.net.au/>

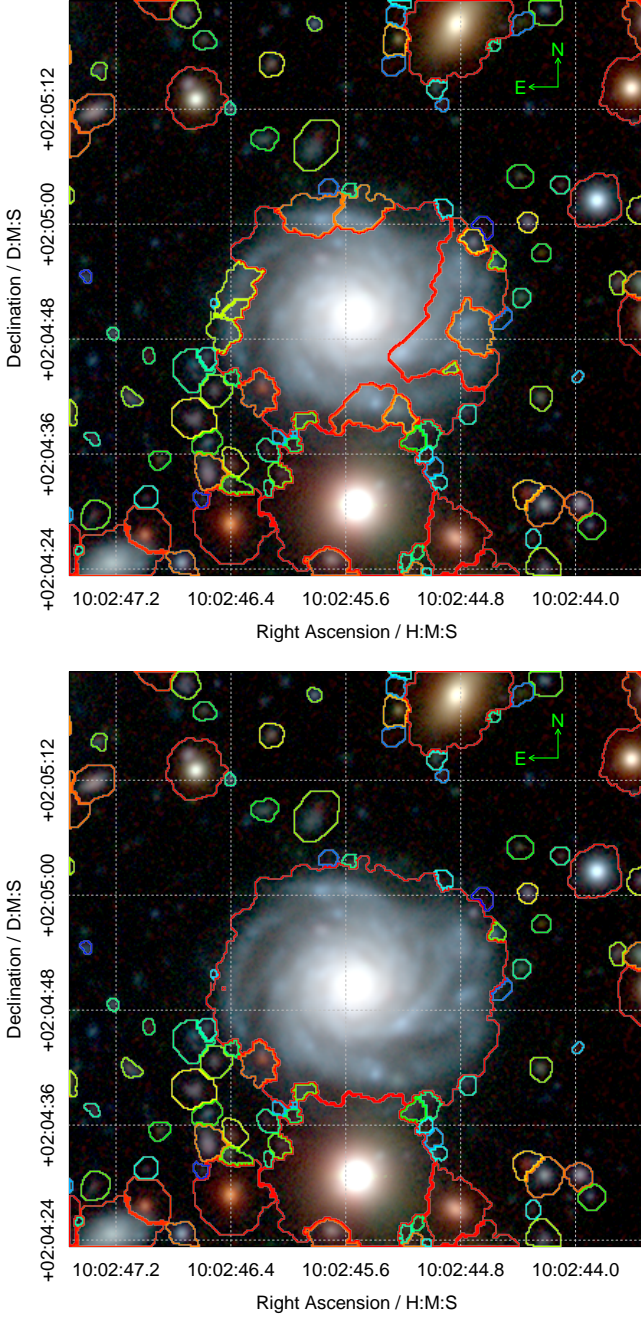


Figure 5. Example of a fragmented galaxy that has been rebuilt. Image shows the ProFOUND segmentation map for a galaxy that has been split into multiple segments. Segments are bounded by colours assigned by the segments flux from blue (faint) to red (bright). The top panel shows the galaxy before regrouping and the lower panel shows the segments after regrouping.

fields. As noted previously, Z-band data does not exist over all of the D03 region and the I-band data comes from different facilities (HSC and VST) in different fields.

Once the stack is produced, ProFOUND then identifies all sources of flux in this stacked image producing a segmentation map designed to separate flux from individual sources (see [Robotham et al. 2018](#), for further details). ProFOUND produces two different segmentation maps, first a colour-optimised segmentation that covers the central

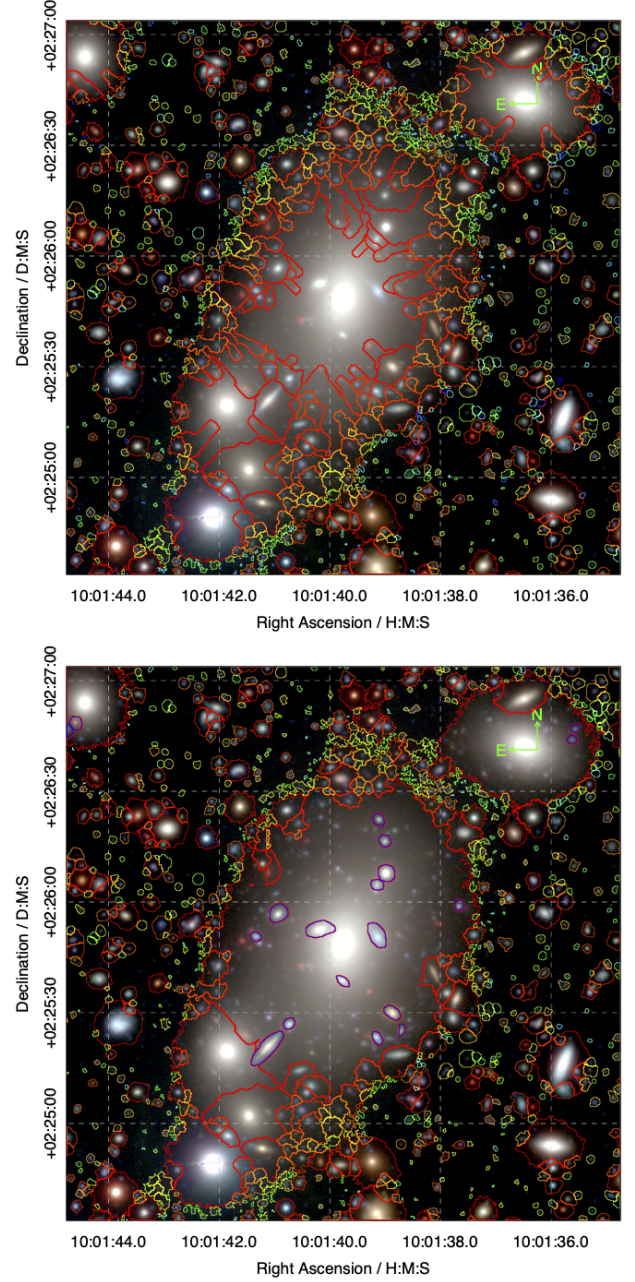


Figure 6. Example of a complex region that required manual intervention to fix segments. The top panel shows the region before manual fixing and the lower panel shows the final segments after manual fixing. Segments which have been manually added, after some regrouping, are bordered by dark blue and red lines and largely fall in the centre of the complex.

high-signal-to-noise region of sources prior to the ProFOUND segment dilation process, and a total-optimised segmentation that dilates the colour-optimised segments in an attempt to extract total flux measurements associated with a source. The colour-optimised segments are essentially tight detection segments (akin to a small fixed-size aperture - but tuned to the shape of the source's central distribution of light), which do not encompass all of galaxy flux. This will best-represent the overall SED shape, but not normalisation. This means that the colour-optimised segments are best used for scientific analyses that do not require total flux measurements (*i.e.* photometric

redshifts), while total-optimised segments are best used for the converse (*i.e.* stellar mass and SFR measurements, etc). Both of these segmentation maps are used in our analysis. For running our ProFOUND source detection we use the Y, J, H band images trimmed to the DEVILS spectroscopic region, but with a 0.1 deg^2 buffer to minimise any issues with sources that overlap the edge of the field. Finally, due to memory issues, ProFOUND can not be run over a full DEVILS field in a single process. To overcome this, we split the field in to a number of overlapping subregions and undertake our photometric detection/measurements in each region independently (8 regions in D02 and also 4 regions in D10 and D03). These are later combined in a process described in Section 5.2. For example, in total ProFOUND identifies $\sim 951,000$ unique segments across our four sub-regions in D10.

While the ProFOUND segmentation map successfully identifies individual sources and robustly maps their extent, a known problem with most automated source finding algorithms (including ProFOUND — but to a lesser degree than *e.g.* SExtractor) is the fragmentation of bright galaxies. This problem has been explored in the derivation of new photometry in GAMA (Bellstedt et al. 2020) and a number of enhancements to ProFOUND were made to assist with fixing this issue. The first two enhancements were the introduction of the ProFOUND- RELTOL and CLIPTOL parameters in the source finding mode. RELTOL allows ProFOUND to keep very extended and flocculent spiral galaxies intact, while having little negative impact on the fainter source deblending that parameters will tend to be optimised for (since this is where almost all of our survey sources exist). CLIPTOL specifies the saddle point flux above which segments are always merged, regardless of competing criteria. This is useful for very bright objects with complex image artefacts (*e.g.* in the regions around bright stars), and allows for proper reconstruction, which might otherwise be hugely fragmented into many small segments. We do however utilise a bright star mask (see Section 5.4), which means that the resulting segments around bright stars are somewhat cosmetic. These new parameters are described in more detail in Bellstedt et al. (2020).

Despite the inclusion of these new ProFOUND parameters, some low-level fragmentation of bright galaxies still occurs. To fix this, and regroup segments belonging to the same bright object, an in-house interactive tool was developed that allows users to view a thumbnail of an object and click on segments to be regrouped. This tool is available through the `profoundSegimFix` function within ProFOUND, and is applied to our total-photometry segments.

As part of its output, ProFOUND provides information on *group* statistics, where a group is defined as touching segments in a *cluster* of segments around a source, or multiple sources (see Robotham et al. 2018). These *group* statistics allow us to easily identify potentially fragmented galaxies in our segmentation maps. Rather than visually inspecting every group, we determine the groups that need to be inspected based on the following criteria:

- i) The group of touching segments must contain at least three segments (this mean that there might be cases where a single galaxy has been split in two and it would not be selected as an object to fix, but because the field is so deep and there are lots of segments there are very few instances where this is the case).
- ii) We only inspect groups with a total group magnitude (across the three stacked detection bands) between 12 and 20.5 mag to reduce the number of groups that needed to be inspected.
- iii) We also only inspect groups where the brightest pixel is at least

500 pixels away from the edge of the frame (this removes groups in our sub-region overlap areas).

- iv) Finally, we also exclude masked objects such as stars and artefacts from the visual re-grouping process, because the majority of touching segments reside in the ghosting surrounding stars.

For example, in the D10 region this resulted in 12,354 groups to visually inspect. Of these, 1,272 required some manual intervention (10.3 per cent). An example of an object whose segments have been regrouped in this way can be seen in Figure 5, where the bottom panel shows the resulting segmentation map after merging. For each of the four input sub-regions, one output file was produced that recorded which segments (as determined by the detection phase of ProFOUND) needed to be regrouped.

In addition to the segment regrouping, upon visual inspection of the ProFOUND outputs, we found that a small number of large, highly clustered sources were merged into a single ProFOUND segment - and thus required *ungrouping*. The `profoundSegimFix` function also allows for segments to be manually created using a GUI tool where the new segments are drawn onto an image. In order to fix all erroneously grouped regions, we first ignore stars, artefacts and masked regions (see below) and then select the superset of segments which are either: i) in the top 100 Y-band brightest segments in their sub-region, ii) in the top 100 Y-band largest segments in their subregion, and iii) objects where the brightest Y-band pixel within a segment in $> 4''$ away from the flux-weighted central pixel of the segment (both provided by ProFOUND). This process visually selected all erroneously grouped regions in our subregions and lead to ~ 30 -60 regions to visually inspect per subregion (*i.e.* there is significant overlap in the selections). Figure 6 shows one of the extremely complex regions in the D10 field that requires both segment regrouping and ungrouping. The top panel show the ProFOUND segmentation map prior to manual fixing, while the bottom panel shows the region following manual fixing. Segments that have been manually included in the ungrouping process are shown bounded by blue/red lines. We note here, that while this process requires manual intervention, it is far less time-consuming than the manual fixing process discussed in Andrews et al. (2017) and Wright et al. (2016).

Once complex regions have been both manually regrouped and ungrouped, where appropriate, we generate a new segmentation map for each subregion and use this for the remainder of the photometry pipeline.

5.2 Multiband Photometry with ProFOUND and Sub-Region Combination

After the initial segmentation map has been defined and manual fixing applied in each of our subregions, these segments are then used to measure both total- and colour-optimised photometry in the UV-MIR bands (GALEX-FUV to *Spitzer*-IRAC $8.0 \mu\text{m}$). Our initial process is only applied to the UV-MIR, where the pixel-scale/seeing are comparable and source blending/confusion between bands is low. The process for measuring our photometry at longer wavelengths using PSF fitting is described in Section 6. Note that in the IRAC bands it is somewhat ambiguous as to which method would be preferred, ProFOUND segmentation versus PSF extraction. As such, we initially perform both approaches for our IRAC photometry and compare to existing MIR measurements for these galaxies. We find that for all of the IRAC bands our ProFOUND segmentation approach provides closer consistency between our new photometry and existing catalogues. Hence, we opt to switch between methods at the

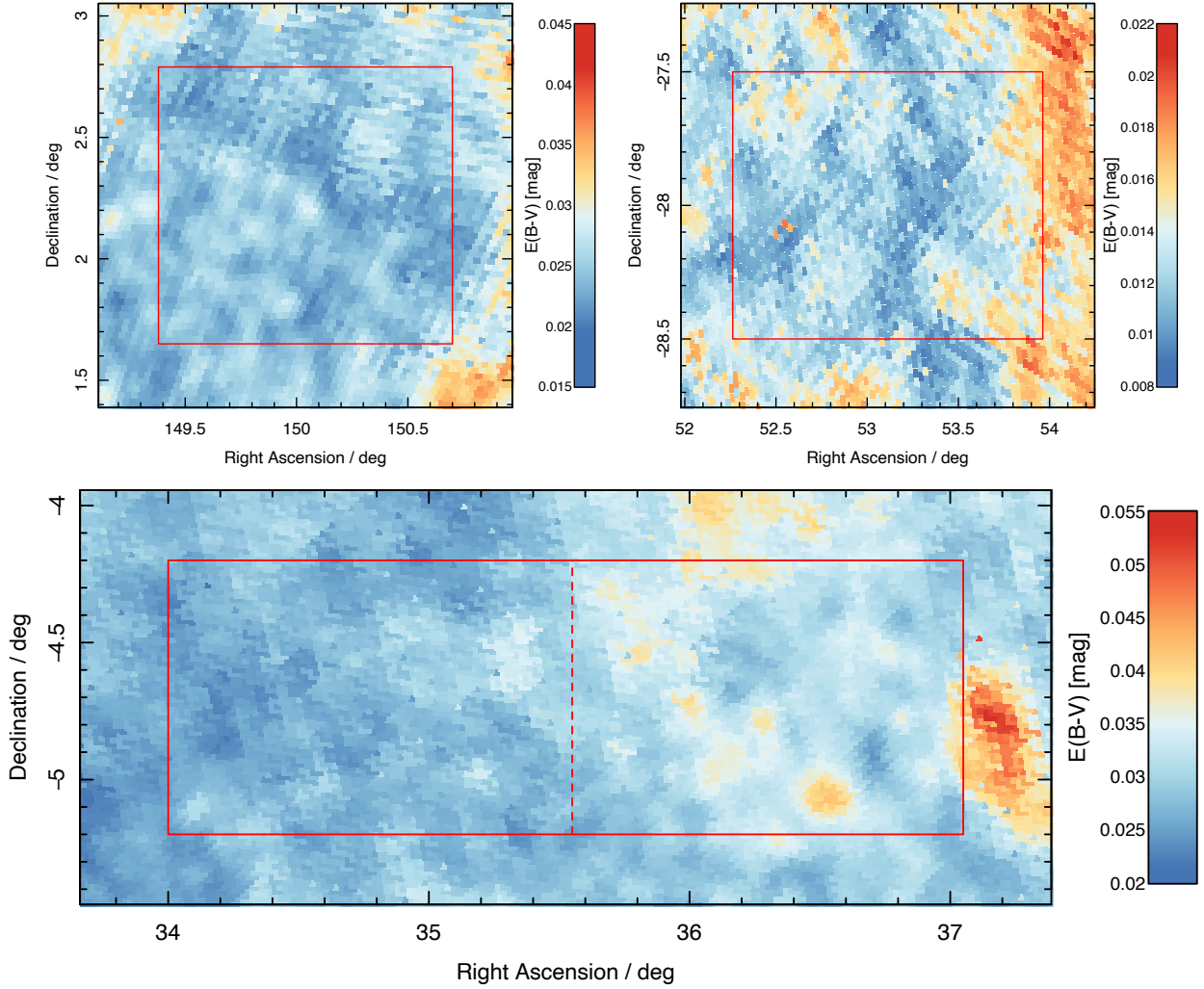


Figure 7. Galactic Extinction in the DEVILS regions based on the Planck $E(B-V)$ maps. Top left = D10, Top right = D03, Bottom = D02. Note that we use a different colour bar scaling for each field as the extinction is low, but significantly different in each region. Thus if the same scale is used, all detail would be removed. The dashed vertical line in D02 displays the separation between the D02A (left) and D02B (right) regions.

IRAC24/MIPS24 boundary. As is shown later, this choice produces tighter MIR colours than the existing photometry catalogues.

Prior to photometric measurements, all imaging bands must first be transformed to the same pixel scale and field size. To do this we use the SWARP package, matching all bands to the same pixel scale and area as the stacked Y, J, and H band image ($0.15'' \text{ pixel}^{-1}$ for UltraVISTA in D10 and $0.2'' \text{ pixel}^{-1}$ for VIDEO in D02/D03). ProFOUND then initially applies the colour-segmentation maps (central high signal-to-noise region) to each band. As the PSF of our imaging varies significantly from band to band, we can not use fixed segments for each filter (as we would miss flux in the lower resolution data). As such, ProFOUND takes the colour-optimised segmentation map as a starting, source detection, point and then allows the segments to further dilate in an attempt to encompass more flux until convergence is reached (see Robotham et al. 2018, for details). This process accounts for the varying PSF, without having to apply detailed modelling of the PSF shape in each band. ProFOUND then outputs both colour and total flux measurements, errors and segment statistics (such as radii, number of pixels, sky background, etc) in each band.

Following measurement in each band, catalogues from our sub-

regions are combined to produce a photometry catalogue for the full DEVILS field. To do this, we combine all sub-regions to a single catalogue, and remove duplicates in the overlapping regions, retaining the source which is closest to its sub-region field centre. We then trim the catalogue to the extent of the DEVILS spectroscopic field. As an example, this results in $\sim 777,000$ unique segments in the D10 region.

5.3 Extinction Corrections

To correct our measured magnitudes for Galactic extinction we use the Planck $E(B-V)$ map⁸, converting HEALpix values to RA and Dec positions across the field. Figure 7 displays the Planck $E(B-V)$ values across the DEVILS regions. For each ProFOUND source we

⁸ HFI CompMap ThermalDustModel 2048 R1.20.fits, https://irsa.ipac.caltech.edu/data/Planck/release_1/all-sky-maps/previews/HFI_CompMap_ThermalDustModel_2048_R1.20/index.html

Table 2. Attenuation values used in conjunction with Planck $E(B - V)$ map, consistent with the local GAMA analysis.

Filter	$[A_x/E(B - V)]$
FUV	8.24152
NUV	8.20733
u	4.81139
g	3.66469
r	2.65460
u	2.07472
Z	1.55222
Y	1.21291
J	0.87624
H	0.56580
Ks	0.36888
S36	0.20124
S45	0.13977
S58	0.10094
S80	0.09818

then identify the closest Planck $E(B - V)$ pixel assigning the corresponding extinction value. We then correct all magnitudes, surface brightnesses and fluxes based on this extinction value. We determine the attenuation correction for each band in the traditional manner (*i.e.* $A_x = [A_x/E(B - V)] \times E(B - V)$) using the extinction coefficients listed in Table 2 (which implicitly use the Galactic extinction law from Schlafly & Finkbeiner 2011). Note that we do not apply any corrections long-ward of the IRAC bands, where emission then arises from dust itself, and would be subtracted as part of the background.

5.4 Masking

As can be seen in the top left panel of Figures 8 (and Figures 2, 3 and 4), our input images have significant issues with ghosting around bright stars. This ghosting is dependent on both position within the focal plane and the brightness of individual stars. In Davies et al. (2018) we developed a method for masking bright stars for the DEVILS input catalogue. However, in this work we have improved our masking procedure to better exclude erroneous sources near bright stars and minimise the area lost to our mask. This process is carried out in a number of stages, which are visually described in Figure 8.

Initially, following the method outlined in Bellstedt et al. (2020) we select all GAIA DR2 stars with GAIA g-band magnitude brighter than 15.75 mag in the DEVILS regions, and define a star exclusion radius which is scaled to the GAIA g-band magnitude, with:

$$r_{star}[r] = 10^{(1.795 - 0.158g_{GAIA})} \text{ and } [r < 1.85', g_{GAIA} < 15.75 \text{ mag}] \quad (1)$$

However, unlike Bellstedt et al. (2020) who use a large conservative radius, our radius is tuned to *just* encompass the ghosting for all stars in our field, excluding the minimum region possible (solid pink circles in Figure 8). All ProFOUND segments within this minimum radius are classified as masked (blue segments in Figure 8). While this masks out the majority of segments in the ghosted region, it does miss some outlying faint segments caused by the ghost. Following this, we then match the GAIA DR2 source positions to our ProFOUND segmentation maps, finding the closest segment centre to the GAIA position (red dots in Figure 8) and defining this as the central stellar segment. As noted previously, ProFOUND fragments very bright sources, and this also occurs for the bright stars. As such,

Table 3. Final unmasked areas in each of our DEVILS regions in the Y-band

Field	Total (deg ²)	Unmasked (deg ²)	Percentage masked
D02	3.04	3.00	1.3%
D03	1.50	1.49	0.7%
D10	1.52	1.47	3.4%

this central segment does not encompass all of the star's flux (or the ghost). We therefore select all segments which are within a *group* (see Section 5.1) with the central GAIA-matched segment and also within $2.2 \times r_{star}$ (dashed pink circles in Figure 8). Segments that match this criteria but are fainter than the DEVILS spectroscopic limit are also masked (red segments in Figure 8). Finally, we class all segments defined as artefacts in the process outlined in Section 5.5 as being masked. The right panels of Figure 8 displays two example regions with all masked segments coloured black, showing that our process effectively removes all erroneous sources of flux in segments across the region. While some remnant of the stellar halo can still be seen, this is not associated with any sources. We then define our masked region as the area contained in masked segment areas. This process results in $\sim 1\text{--}3\%$ of each field being masked, with our final unmasked areas given in Table 3. For comparison Bellstedt et al. (2020) report 5.4% of the GAMA area is masked using their process. Note that the masked percentage within D10 is larger as the deep UltraVISTA data has larger haloes around bright stars (see Y-band panels in Figures 2, 3 and 4). We retain all ProFOUND-detected segments in our final catalogues, but assign a MASK=1 flag to sources that have been masked.

5.5 Object Classification

5.5.1 Star, galaxy and ambiguous classification

In order to separate stars and galaxies, we perform a multi-stage process using the ProFOUND-derived outputs. This process is detailed in Figure 9 - showing just sources for the D10 region. First we consider two separate parameter spaces, Y-band R50 (the radius containing 50% of the source's Y-band flux in arcsec) vs. Ymag, and (H-Ks)-(Y-J) vs. Ymag, displayed in the left and right columns of Figure 9, respectively. In the top panel of Figure 9 we colour-code each of our sources by the SED-derived source type, as estimated from the COSMOS2015 catalogue via the photometric redshift fitting code *Le Phare* (where available), with the middle panels displaying the gridded galaxy fraction. Using these we define an ambiguous region where galaxies and stars are largely indistinguishable in each parameter space (bounded by the dashed and dotted lines) - *i.e.* there are roughly equal numbers of galaxies and stars. Sources that are above the dashed line in either parameter space are classed as galaxies, and sources below the dotted line in either parameter space are classed as stars. Sources that fall in between these two classification in both planes are flagged as 'ambiguous', and sources that are classified as a star in one plane and a galaxy in the other are also classified as 'ambiguous'. The equations that define the lines are:

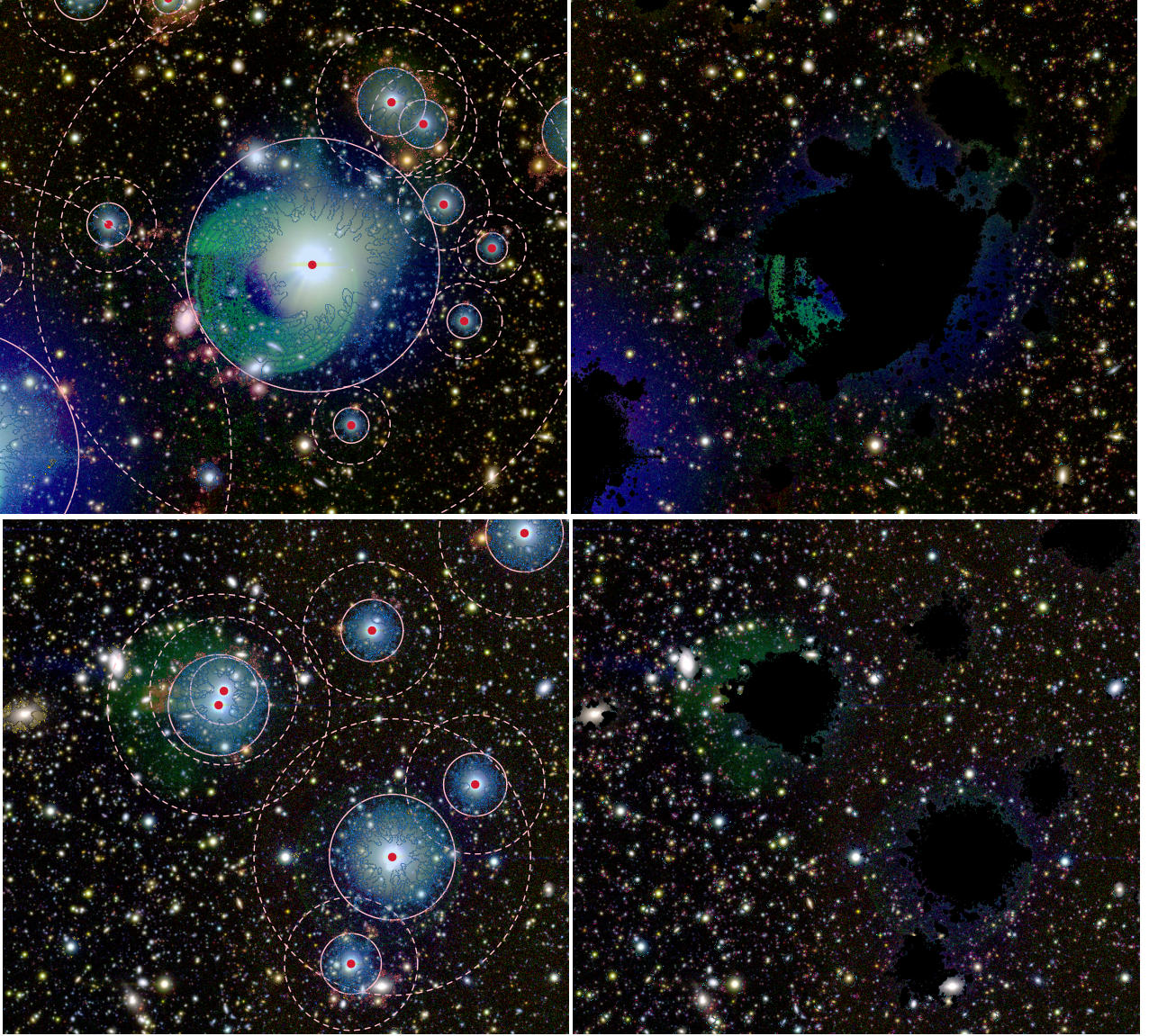


Figure 8. Example of the masking procedure overlaid on a H (VISTA), Y (VISTA), r (HSC) RGB image (note that only the H and Y bands are used in our source detection stacked image, so blue extended emission does not contribute to our source detection). Left: ProFound segments are either masked or identified as artefacts using three different methods. Firstly a GAIA star mask is used to define an exclusion radius around bright stars (pink solid circle). This radius is scaled to the GAIA g-band magnitude (see Section 5.4). All segments within this radius are flagged as being masked (blue-segments). Secondly, we define a region of $2.2 \times$ the GAIA radius (pink dashed circle). Segments within this region that are contained within the same ProFound group as the central star and are fainter than the DEVILS spectroscopic limit ($Y > 21.2$) are also flagged as masked (red-segments). Finally, we also identify additional artefacts using the procedure outlined in Section 5.5 - which are coloured orange. Right: The results of masking process. Here all masked segments are coloured black. We highlight all $Y < 24.0$ mag segments in magenta, and $Y < 21.2$ mag (the DEVILS spectroscopic limit) segments in blue, showing that the masking process only retains segments where robust photometry can be derived.

Galaxies (dashed lines):

$$R_{50} > -28.49 + 9.52Y - 1.03Y^2 + 0.05Y^3 \\ -0.0011Y^4 + 8.4e^{-6}Y^5,$$

$$(H - K_s) - (Y - J) > -0.15 \quad \text{if } Y < 22.2, \\ (H - K_s) - (Y - J) > -0.15 - 0.03(Y - 22.2)^5 \quad \text{if } Y > 22.2$$

Stars (dotted lines):

$$R_{50} < -161.33 + 44.89Y - 4.75Y^2 + 0.24Y^3 \\ -0.0061Y^4 + 5.9e^{-5}Y^5,$$

$$-0.7 < (H - K_s) - (Y - J) < -0.15 \quad \& \quad Y < 21.75 \\ \text{OR } Y < 16$$

The bottom panels of each column in Figure 9 show our final classifications as either star, galaxy or ambiguous in the D10 region, with the number of sources in each category displayed in the legend.

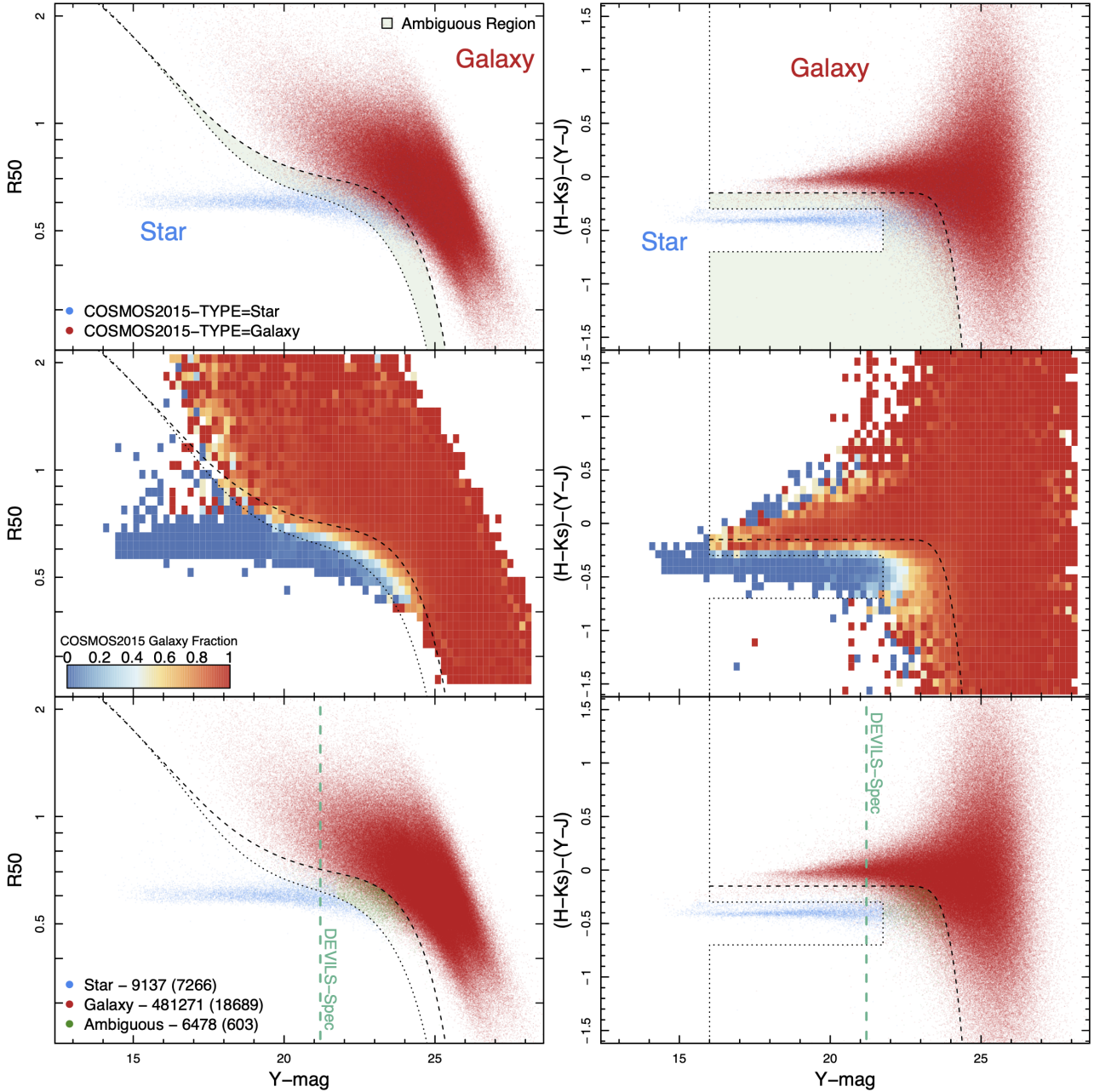


Figure 9. Star-galaxy separation using measured half-light radius versus Y-band magnitude (left) and (H-Ks)-(Y-J) colour versus Y-band magnitude (right) in the D10 region. The top panels display the distribution of sources in our photometric catalogue colour coded by the source type assigned via the photometric redshift fitting code *Le Phare* in the COSMOS2015 catalogue. The middle panels show the same data, but binned and colour-coded by the fraction of galaxies in each bin. We use these figures to define selection boundaries between galaxy/ambiguous (dashed lines) and stars/ambiguous (dotted line). We then determine the stars, galaxies and ambiguous sources, based on the dual selection in both planes (bottom row). These lines and the relevant selections are described in Section 5.5.1. The DEVILS spectroscopic limit is shown by the dashed vertical line in the bottom row. Values in the legend are the number of sources in each category in the D10 region for the full samples, and just to the DEVILS spectroscopic limits in brackets. *i.e.* to the DEVILS spectroscopic limit $\sim 27\%$ of sources are stars and just $\sim 2\%$ are ambiguous. These numbers are similar in D02 and D03.

Within our final catalogues these classification are delineated by the STARCLASS value as either 0 (galaxy), 1 (star), or 2 (ambiguous). The same selection is applied to sources in both D02 and D03.

5.5.2 Artefact Flags

In addition to flagging of galaxies and stars, we also identify potential artefacts in our photometry catalogues, where flux is not associated with an astronomical source, in a similar method to Bellstedt et al. (2020). This is done in a number of different ways with artefacts

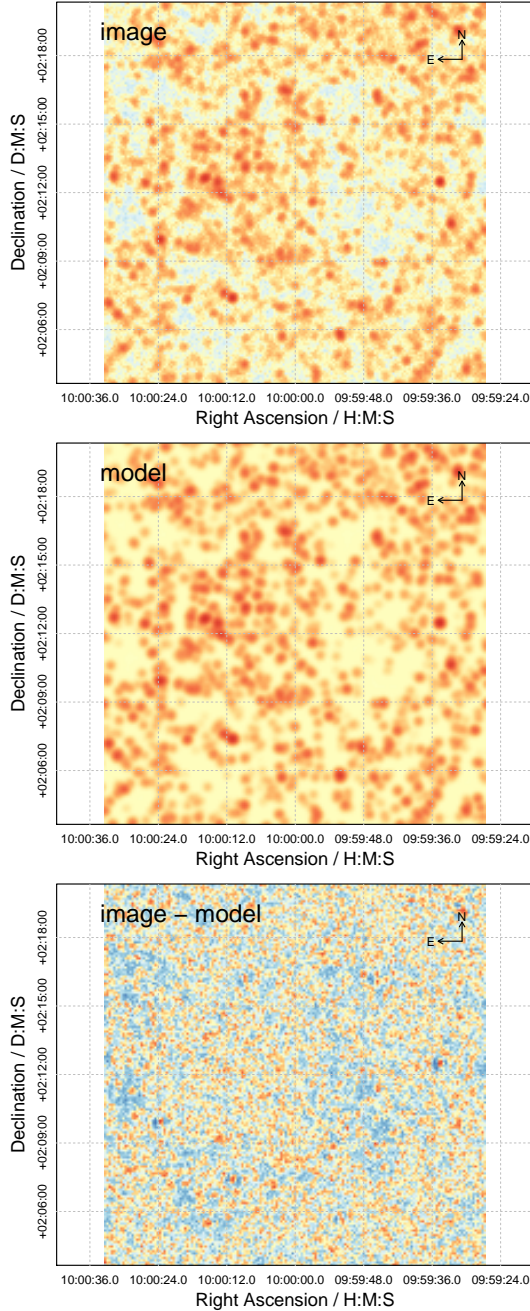


Figure 10. Example of the photometry extraction in the SPIRE 250 band. The top panel shows the original image, and the middle panel shows the ProFOUND-produced model of the objects. The residual when subtracting the model off the image is shown in the bottom panel.

flagged as segments that meet one of the following criteria: i) the source is only detected in one of the g, r or i bands and not the others; ii) the source is only detected in one of the z, Y, J, H, Ks bands and not the others; iii) the source's Y-band R50 is $< 0.15''$ (smaller than half a pixel); or iv) the source's r-z colour is < -0.75 mag (unphysical colour). These sources are kept in our final catalogues but delineated with `ARTEFACTFLAG=1` (all other sources have `ARTEFACTFLAG=0`). As an example of the artefacts in our data, `ARTEFACTFLAG=1` segments are displayed in orange in the left column of Figure 8.

Table 4. ProFOUND Options used for FIR photometry for each instrument. For details of each of these parameters and how they affect source detection, see Bellstedt et al. (2020).

ProFOUND Option	MIPS 24/70	PACS	SPIRE
fit_iters	5	5	5
pixcut	3	3	3
skycut	2	2	2
ext	1	1	1
redosky	FALSE	FALSE	FALSE
psf_redosky	TRUE	TRUE	TRUE
iters	4	4	4
tolerance	1/0	0	0
sigma	2	2	0
magdiff	5	5	5

5.6 Differences to the original DEVILS target input catalogue

In Davies et al. (2018) we have already discussed the use of ProFOUND to generate the initial spectroscopic targeting catalogue for DEVILS in the NIR. While our approach is very similar here (but expanded to a broader wavelength range), there are notable changes designed to make our photometric measurements more robust. The process outlined in Davies et al. (2018) was somewhat conservative and designed to produce robust photometry for the bright ($Y < 21.2$ mag) spectroscopic sample for DEVILS at the start of spectroscopic observations. Here we have improved upon this process in order to both provide more robust measurements for our spectroscopic input catalogue and to produce photometric measurements to faint magnitudes for additional science.

Firstly, we now use updated versions of both the UltraVISTA and VIDEO data that were made available following Davies et al. (2018). Secondly, we have performed the segmentation fixing outlined in Section 5.1 to fix larger, extended sources. This was not applied in Davies et al. (2018) and has improved the photometric measurements for sources at the bright end. Thirdly, we have improved our masking process based on the experience of Bellstedt et al. (2020) in producing the GAMA photometry catalogues. Within Davies et al. (2018) we used a masking procedure based on the ProFOUND skymean measurements. This was found to miss some halo regions around bright stars and over-mask other regions. Our new method improves upon this and reduces the fraction of the fields that required masking but still removes erroneous sources. Finally, we also improved our star-galaxy separation method. Previously we only used a simple NIR colour separation between stars and galaxies. While this works well for bright systems (which we are targeting spectroscopically) it fails at fainter magnitudes, hence we apply a more complex method here. However, it is worth noting that these methods are essentially identical at the bright ($Y < 21.2$ mag) end.

While there are significant changes between the method outlined in Davies et al. (2018) and the method used here, this has in fact very little impact on the photometry for our spectroscopic sample (modulo the addition of some new un-masked objects). The spread (σ) of Y-band photometric difference between the target catalogue outlined in Davies et al. (2018) and that described here is ~ 0.1 mag. However, in order to use the best available photometry for our spectroscopic sample, we now update to our new photometry and have transitioned to the new input catalogue for our observations based on the catalogues discussed here.

6 MIR-FIR PHOTOMETRIC MEASUREMENTS

Once our UV-MIR catalogues and flags are in place, we then extract photometry in the MIR-FIR using, once again, a similar method to that of Bellstedt et al. (2020). Due to the shallower depth, poorer resolution and the existence of FIR bright sources that are undetected in the optical-NIR, it is not appropriate to directly apply our NIR-defined segmentation map to the MIR-FIR data in a similar manner to the shorter wavelength bands. To overcome this, ProFOUND has an inbuilt `profoundFitMagPSF` function specifically defined for the measurement of photometry in low-resolution, shallow data (*i.e.* the MIR-FIR). This method uses the known source positions, here provided from our optical-NIR catalogues, to fit the PSF of each MIR-FIR band to the images, iterating by applying an expectation maximisation function. This process is described extensively in Bellstedt et al. (2020) but briefly, in each band independently the function extracts flux at the positions of an object catalogue, and then iterates over the flux of each object to ensure that all non-sky flux is accounted for in the image and sources are not over extracted. For each band, the locations of our NIR-selected objects provide the coordinates at which to place a PSF and extract flux in the longer wavelength data. However, it is inappropriate to include all of our NIR-selected sources to faint magnitudes because i) Y-flux is not well correlated with the expected emission at longer wavelengths and ii) the lower resolution of the MIR-FIR data means that sources will be heavily confused with multiple input galaxies occupying the same resolution element. As such, we must first apply appropriate cuts to our NIR-selected catalogue to provide sensible input positions for our MIR-FIR analysis.

For this, we first run `profoundFitMagPSF` on the MIPS24 images, using a $Y < 21.2$ mag sample from our UV-MIR catalogue, excluding masked objects and objects classified as stars or artefacts (for example, this results in 17,209 objects for D10). `profoundFitMagPSF` not only measures source photometry for the input sample, but also identifies any additional sources for flux from objects not aligned with the input catalogue (*i.e.* NIR-faint systems). In the MIPS24, a large fraction of sources (28% in D10) are not associated with a $Y < 21.2$ mag source, these sources are then matched back to the full UV-MIR catalogue using both on-sky positional offset (with a maximum matching radius of $5''$) and expected $Y-24\mu\text{m}$ colour. To estimate the expected $Y-24\mu\text{m}$ colour we take all $Y < 21.2$ mag matches and find the typical $Y-24\mu\text{m}$ colour to be 3 mag. We then perform a 3D spherical match between MIPS24 sources and our UV-MIR catalogue using on-sky separation and $(Y-24\mu\text{m})-3$ colour offset. *i.e.* for each UV-MIR source within $5''$ of a MIPS24-detected position, we assign a probability of correct match based on the sky separation and the expected $Y-24\mu\text{m}$ colour, and take the most likely match. As such, we implicitly assume that all MIPS24 sources are contained within our UV-MIR catalogue, and that all sources should have the typical $Y-24\mu\text{m}$ colour. This process will potentially fail for AGN-like sources which may have atypical $Y-24\mu\text{m}$ colours, but these are likely to only form a small fraction of the source sample. We note that not all MIPS24-detected sources are matched to a UV-MIR catalogue source using this method, these are retained as true NIR-faint and MIPS24-bright sources.

To build our input source positions for longer wavelengths, we combine our $Y < 21.2$ mag sample with the MIPS24-detected matched sample as described above and the additional sources which are unmatched in the UV-MIR catalogue. Using these input objects, we run `profoundFitMagPSF` on all of the 70-500 μm bands. To account for potential previous over-subtraction of the sky in the data reduction phase of the FIR imaging by the original teams (possibly

due to the confused nature of sky pixels), we also include a second phase of extraction with an explicit sky subtraction using the sky value as measured by ProFOUND in the first phase.

For completeness the `profoundFitMagPSF` settings used in our analysis are shown in Table 4. `profoundFitMagPSF` accepts an empirical PSF provided by the user in various forms. Here we use the observed PSF kernels from PEP for the PACS bands⁹, and a Gaussian PSF for the SPIRE bands using the FWHM as given in Oliver et al. (2012) (18.15, 25.15, 36.3 arcsec for the 250, 350 and 500 μm bands, respectively). For the MIPS bands, we use the 100 K PSFs from Gordon et al. (2008) and re-scale the PSF to the image pixel scale. While measuring flux, we apply multiplicative aperture corrections of 1.15 for MIPS 70 (Frayer et al. 2009), 1.50 for PACS 100 and 1.477 for PACS 160, and an additional multiplicative high-pass correction of 1.12 and 1.11 for PACS 100 and 160, respectively, as suggested by the PACS data release⁹.

The fraction of $Y < 21.2$ mag objects with detections (arbitrarily defining a detection as having a measured magnitudes of < 30 mag) varied in each band depending on the depth of the imaging. For example, in D10 the $M24/M70/P100/P160/S250/S350/S500\mu\text{m}$ bands, 81.1/44.4/55.8/57.1/62.5/44.4/28.3 per cent of objects had detections, respectively. 1494 objects had detections in all seven bands, corresponding to 8.6 per cent of the $Y < 21.2$ mag sample. No objects were undetected in all of the seven bands.

The resulting uncertainties, due to the expectation maximisation mixture modelling process, accurately reflect the inherent uncertainties in this process. If two optically-detected sources are close in projection, then the uncertainty will reflect the potential confusion between these two sources. In Figure 10 we show an example of an original image, final modelled image, and resulting residual in the SPIRE 250 μm band in D10.

In addition to the objects detected in the FIR with optical/MIR counterparts, a small fraction of FIR objects were detected with no clear counterpart - *i.e.* objects which are not detected in MIPS24 but are detected at longer wavelengths - likely high redshift FIR-bright systems. The outputs for these additional sources are saved, but not included in our DEVILS photometry catalogue (as they are not associated with a DEVILS target). However, we do add these sources into the catalogues used to generate the deep number counts presented in this work.

7 VERIFICATION OF PHOTOMETRY

In the following section we carry out a number of verification checks to assess the validity of our current photometry catalogue. Here we present these comparisons just in the D10 region, where more extensive existing data is available, to highlight the validity of our process. However, similar checks are performed on all regions with similar results. These tests are intended to provide the reader with the confidence that our new photometry is robust, and can be used for future science projects.

7.1 Comparisons to Previous Photometry in the COSMOS Field

First we compare our total photometry measurements to existing photometry catalogues in the COSMOS region. We do not assume any particular catalogue is the ground truth, but simply highlight the

⁹ http://www.mpe.mpg.de/resources/PEP/DR1_tarballs/readme_PEP_global.pdf

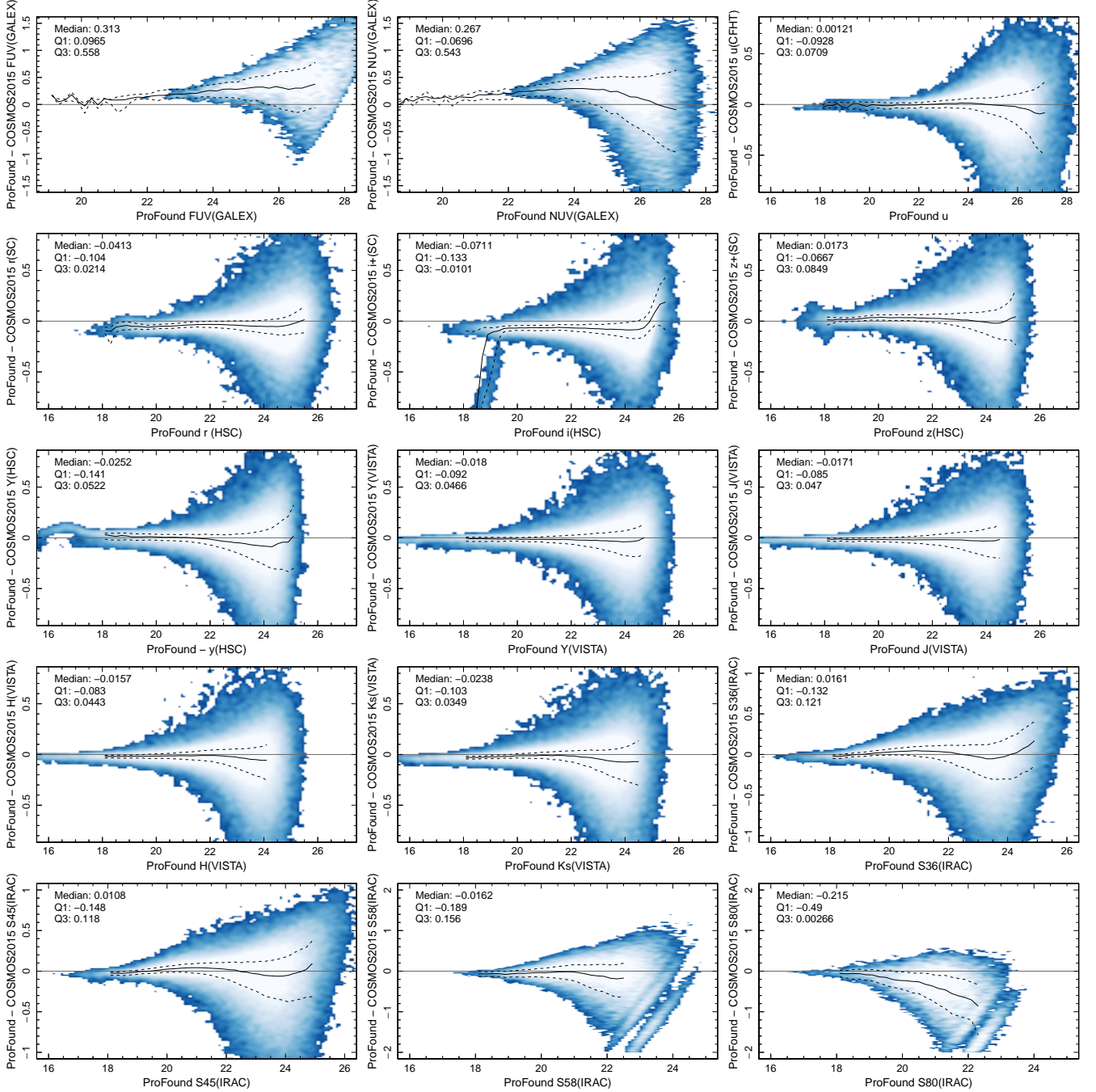


Figure 11. Comparison between our new ProFound photometry and COSMOS2015 catalogue. Each panel displays ProFound-COSMOS2015 for $2''$ matched sources. Note that in r, i and z bands we compare HSC with Subaru SuprimeCam, and in VISTA Y, J, H and Ks bands we compare UltraVISTA DR4 with DR2. Solid and dashed lines show the running median and interquartile range of the data, respectively. The full sample median and ranges are noted in each panel. Note that these do not have MW extinction corrections applied to be comparable to the public COSMOS2015 catalogue. Note that COSMOS2015 does not provide g-band measurements, and as such no comparison is shown here. Note, the diagonal feature in the i-band for both this figure and Figure 12 are caused by saturated sources in the old SuprimeCam data used in both COSMOS2015 and G10/COSMOS.

consistency (or lack thereof) between photometric measurements using different techniques.

In Figure 11 we compare our UV-MIR photometric measurements with those from the COSMOS2015 catalogue of Laigle et al. (2016). Briefly, Laigle et al. (2016) uses SExtractor (Bertin & Arnouts 1996) to derive total and fixed aperture photometry from

the Optical-NIR multi-wavelength data in COSMOS. These are then catalogue matched to the UV and longer wavelength data available in the region - please refer to Laigle et al. (2016) for further details. Here we first compare to the total (MAG_AUTO) measurements where available. We note that the imaging used in this work and Laigle et al. (2016) catalogue is identical except for the following:

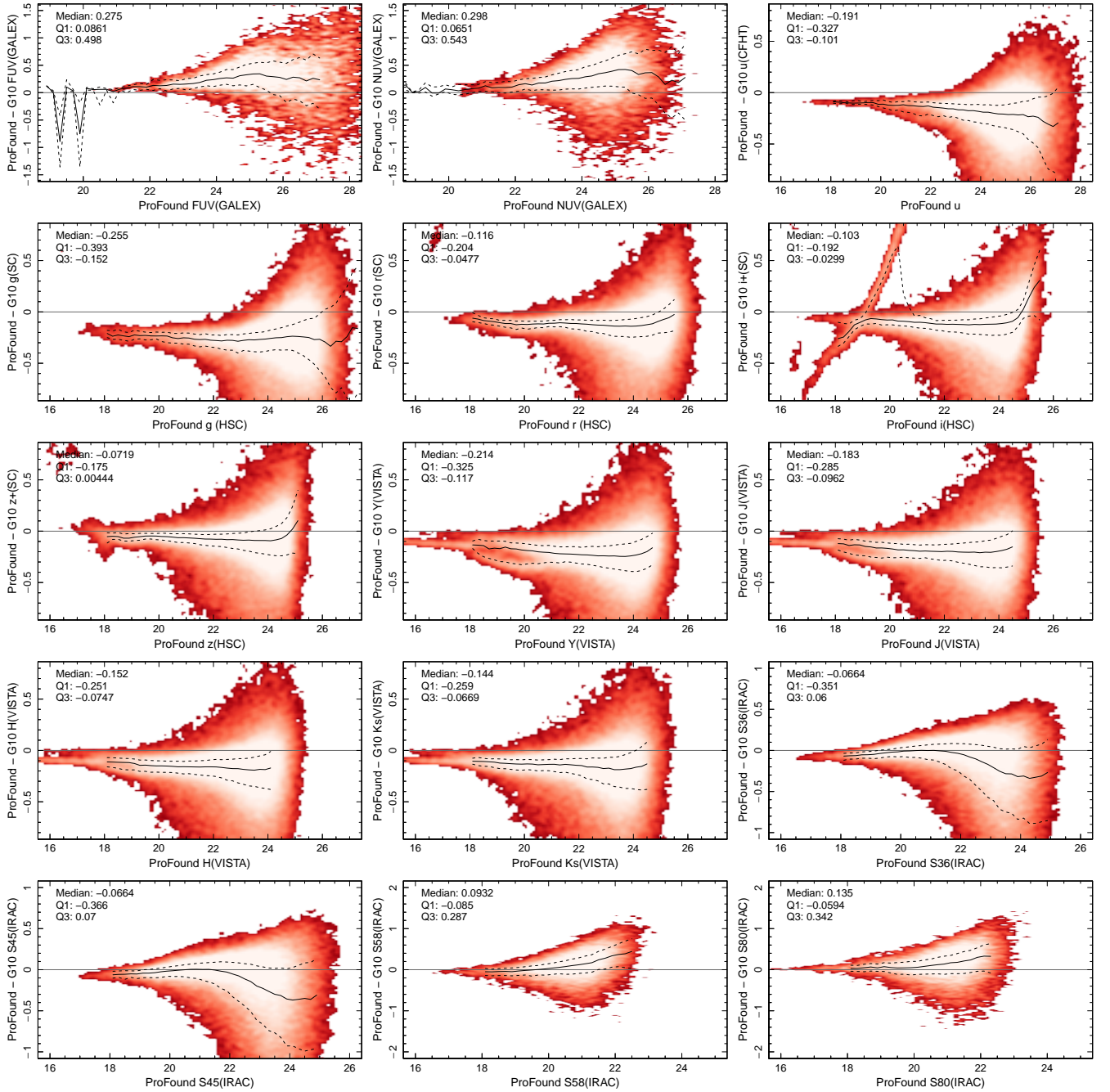


Figure 12. Same as Figure 11 but for the G10/COSMOS catalogue. However, these have MW extinction corrections applied to be comparable to the public G10/COSMOS photometry. Note that in r, i and z bands we compare HSC with Subaru SuprimeCam, and in VISTA Y, J, H and Ks bands we compare UltraVISTA DR4 with DR2

we have used newer HSC data in g, r, i, z bands in comparison to the Subaru SuprimeCam data used in COSMOS2015, and we use UltraVISTA DR4 while COSMOS2015 uses UltraVISTA DR2. In Figure 11 we also compare photometry prior to galactic extinction correction being applied, as this is how the raw COSMOS2015 photometry is provided. We find only very small median offsets in the majority of bands (<0.1 mag), showing consistency between our measurements, with the exception of the GALEX bands that show a normalisation offset of $\sim 0.25 - 0.3$ mag. This is discussed further in

Section 7.2. However, we find that our photometry and that derived in COSMOS2015 is largely consistent despite using different methods, and in some cases, different data sets. However, our new photometry will not suffer from some of the issues discussed previously (and extensively in Robotham et al. 2018) and is more robust for extracting total photometry measurements.

Next we compare our UV-MIR photometry to the G10/COSMOS catalogue of Andrews et al. (2017) in Figure 12. The G10/COSMOS catalogue uses the Lambda Adaptive Multi-wavelength Analysis for

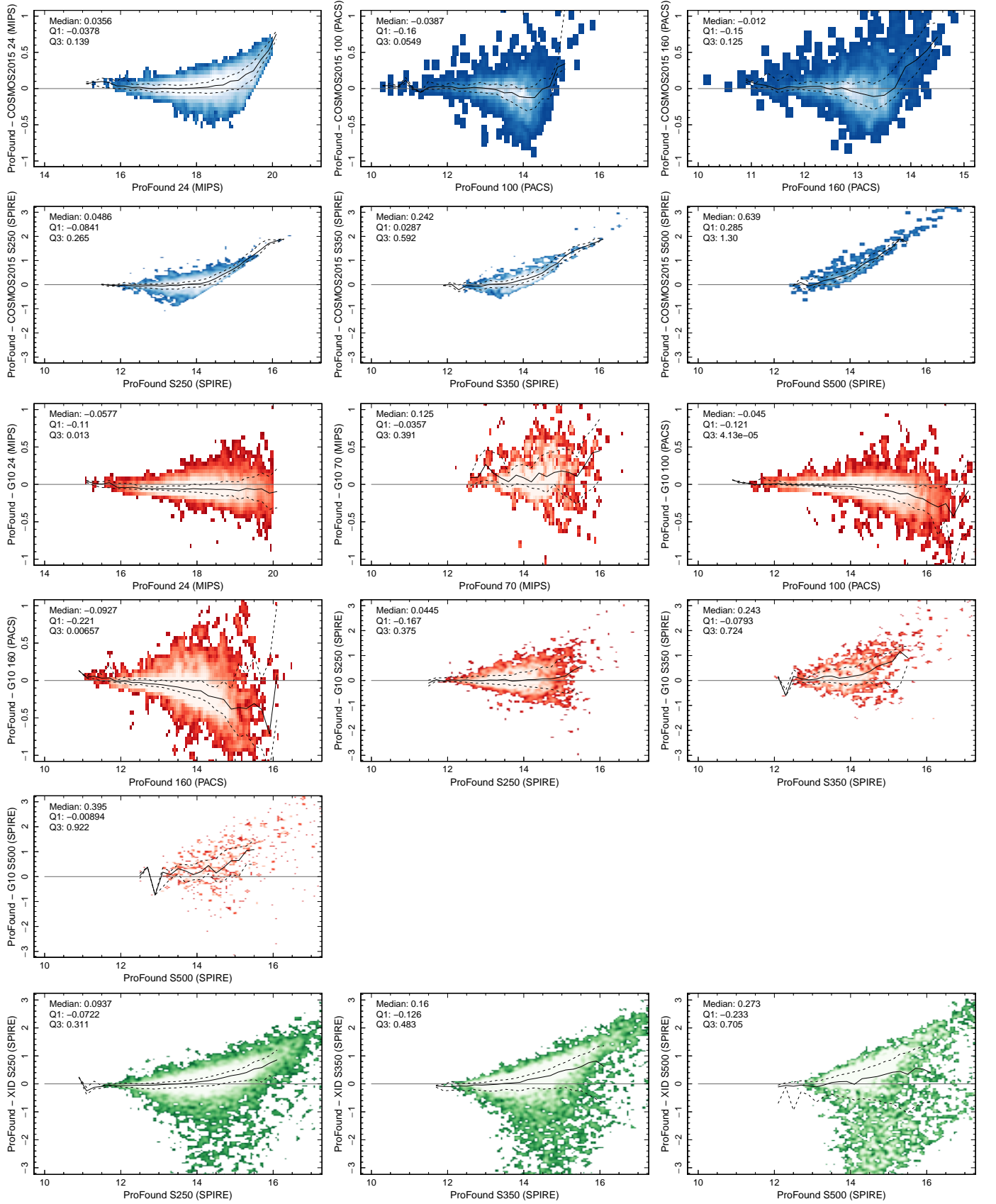


Figure 13. Same as Figure 11 but showing comparisons between our new MIR-FIR ProFound photometry and COSMOS2015 (blue), G10/COSMOS (red) and XID+ (green) catalogues, where available, in the MIR-FIR regime.

R (LAMBDAR, Wright et al. 2016) code with identical imaging datasets to COSMOS2015. The LAMBDAR software starts with base apertures defined by SExtractor, but within Andrews et al. (2017) they go through an extensive processes of manually fixing any erroneous apertures. Firstly, in Figure 12 we see comparable median offsets to the COSMOS2015 catalogue in the GALEX UV bands, once again this is discussed further in Section 7.2. Through the u-Ks bands, we see normalisation offsets of up to ~ 0.3 mag, particularly in the VISTA NIR bands. These are consistent with the offsets between G10/COSMOS and COSMOS2015 presented in Andrews et al. (2017). In Andrews et al. (2017) it was argued that these offsets are likely due to the initial aperture definitions and/or choice of selection band. However, given that our new ProFOUND photometry does not rely on apertures for photometry, and we agree more closely with the COSMOS2015 catalogue in the NIR, this is unlikely to be the case and the G10/COSMOS measurements are simply missing flux and/or have a zero-point error. We do agree very well with IRAC MIR measurements from G10/COSMOS with < 0.1 mag median offset in all bands.

For our MIR-FIR photometry, we again compare to COSMOS2015 and G10/COSMOS, but also to the XID+ SPIRE catalogues of the *Herschel* Extragalactic Legacy Project (HELP) team (see Hurley et al. 2017). All comparisons are presented in Figure 13. We find good agreement with all existing photometry in the *Spitzer* and, *Herschel* PACS and SPIRE data - suggesting our photometry is consistent with existing catalogues. We highlight that while we are consistent with these existing catalogue across their individual regimes, the benefit here is that we are using a single consistent package to extract photometry across the full wavelength range, removing some of the issues associated with catalogue matching of data. We have also optimised our catalogues to robustly measure total flux measurements across all sources, which are required for robust measurements of galaxy properties such as SFRs and stellar masses (see Thorne et al. 2020).

7.2 Photometric Offsets

As discussed in the previous section, while our photometric measurements are largely consistent with existing catalogues we do see a number of small median zero point offsets. These are most significant in the GALEX-UV bands. However, the methods used to calculate the photometry in these bands is vastly different between our new work and the existing catalogues, and a detailed assessment of the previous photometry finds a number of seemingly arbitrary zero-point corrections are applied to the photometry in these bands. As such, we do not know which catalogue now presents the ground truth.

To test this, we use the ProSPECT (Robotham et al. 2020) spectral energy distribution (SED) fitting results outlined in Thorne et al. (2020). Thorne et al fit all DEVILS D10 galaxies using our new photometry to produce a robust SED fit and derive star-formation histories, stellar masses, SFRs, etc. For our tests we then also fit the existing COSMOS2015 photometry (which shows the similar offsets as G10/COSMOS - particularly in the UV bands) for a random sample of $\sim 24,000$ DEVILS galaxies with spectroscopic redshifts at $z < 1$, and using the same ProSPECT parameters as Thorne et al. Here we use the best-fit ProSPECT SED and compare to the input photometric measurements, for both ProFOUND total photometry and the COSMOS2015 photometry. For COSMOS2015 we use the $2''$ aperture photometry measurements to maximise robust SED shape fits, *i.e.* aiming to obtain the best possible fits. We also note here that the COSMOS2015 sample already apply per-band zero-point offsets

using the LePHARE SED fitting code in order to improve the accuracy of their photometric redshifts. As such, their photometry should be tuned to closely match the overall SED shape of existing galaxy templates. However, systematic offsets between the ProSPECT fit and input photometry can highlight potential zero-point offsets in a given photometric band, assuming the suite of SED models is representative of the true galaxy population. Figures 14 and 15 display the input photometric measurement minus the ProSPECT best-fit SED measurements for all bands. In each panel we note the median offset of each distribution, the offset from the peak of a Gaussian fit to the distribution and the peak position offset for both photometry catalogues as a measure of any systematic differences between the photometric catalogues and ProSPECT SED models. We find no significant residual offset between our ProFOUND photometry and the ProSPECT best-fit SED in the GALEX bands, or in fact any others. There is a slight offset in the HSC g-band (~ 0.07 mag), which we believe is due to the 4000\AA break falling within this band at the redshift of a typical DEVILS galaxy and the ProSPECT models not completely encompassing the true range of galaxy types at this point. When the full Thorne et al. (2020) sample (including photometric redshifts) is fit using a broader redshift range, this offset disappears. However, we do see numerous offsets for the COSMOS2015 photometry when fitted using ProSPECT, in multiple bands in Figure 14 in the NUV, z, H, Ks and IRAC channels. This suggests that our new photometry is more consistent with realistic galaxy SEDs (at least those probed by ProSPECT). We also display the outlier fraction, defined as the fraction of sources that are outside the offset peak value from ProFOUND/COSMOS2015 $\pm 2 \times$ the standard deviation of the ProFOUND distribution. We find that the COSMOS2015 photometry has larger outlier fractions in almost all bands (modulo u, i, Y and S500 where the offsets are comparable). This further suggests that measured scatter in our new photometry is smaller when compared to the ProSPECT SED models. In combination, these results suggest that any differences in zero point between our new photometry and the COSMOS2015 catalogues is unlikely to be due to errors in our current approach.

7.3 Colour Comparisons

While the figures displayed in previous sections are useful for diagnosing zero-point and linearity problems (*i.e.* magnitude-dependent offsets), they do not give an objective assessment as to which data set is more robust in terms of the photometry measurement process. One potential avenue to explore this is through galaxy colours in adjacent filters. A sample of galaxies will have some intrinsic colour distribution, which is then convolved with error distributions introduced by the instrumentation, observing conditions, photometric data reduction methods and photometric measurement error. A narrower colour distribution and a lower outlier fraction thus indicating a narrower photometric error distribution are, hence, likely more reliable.

To explore the colour distributions of our sample we first measure the colours in adjacent bands for a $2''$ matched sample of $Y < 24.5$ mags galaxies in the D10 region, for FUV-S80, and sources brighter than the 5σ detection limit, for MIPS24-S500, for ProFOUND, COSMOS2015 and G10/COSMOS. Here we use the colour-optimised photometry from ProFOUND and fixed $2''$ (colour-optimised) photometry from COSMOS2015 (for G10/COSMOS only total photometry is provided). For each distribution we measure the interquartile range and outlier fraction (defined as the number of sources which are > 0.5 mag outside of the interquartile range) for each catalogue and in each band.

Rather than showing the raw distributions, to better illustrate these

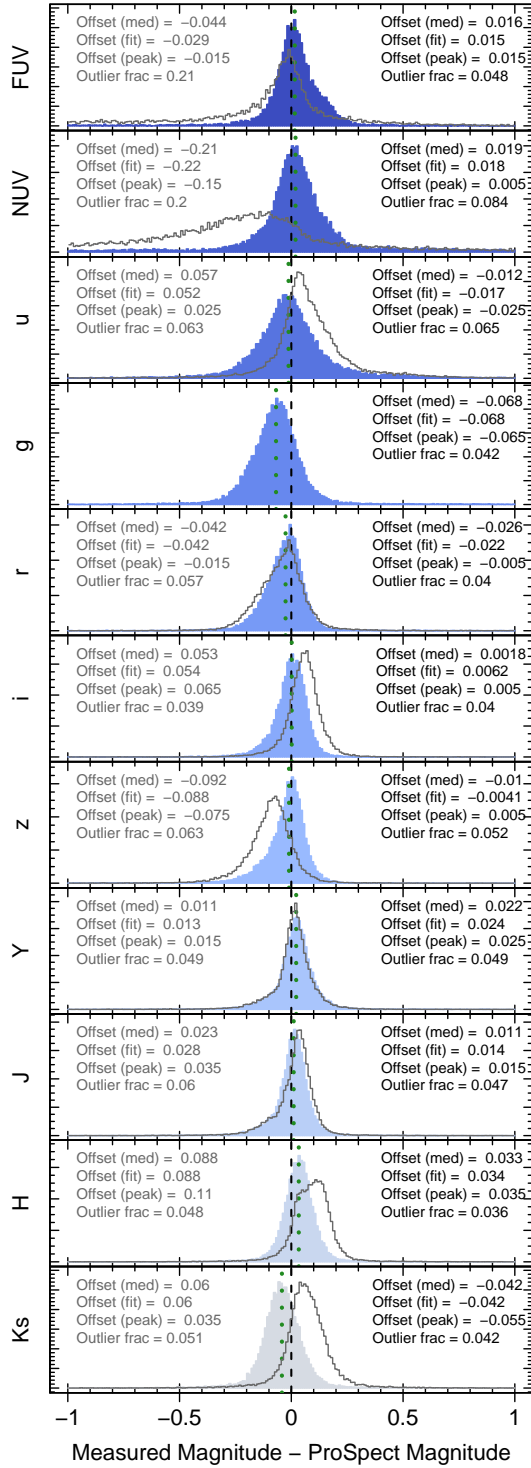


Figure 14. Individual band offsets between measured photometry for a random sample of 24,000 D10 galaxies and the ProSPECT best fit SED in FUV - Ks. Coloured filled histograms and right-hand legend show our new photometry. Grey lines and left hand legend show COSMOS2015 photometry. In the legends we display the offset values measured in three different ways, where large absolute values indicate a larger discrepancy with the ProSPECT SED models (see text for details). In most bands our new photometry has smaller offsets using all methods. We also show the outlier fraction (see text for details), where our new photometry has comparable or smaller values in every band. The dashed vertical line display the zero offset line, while the dotted green line shows the peak of the ProFOUND-derived distribution.

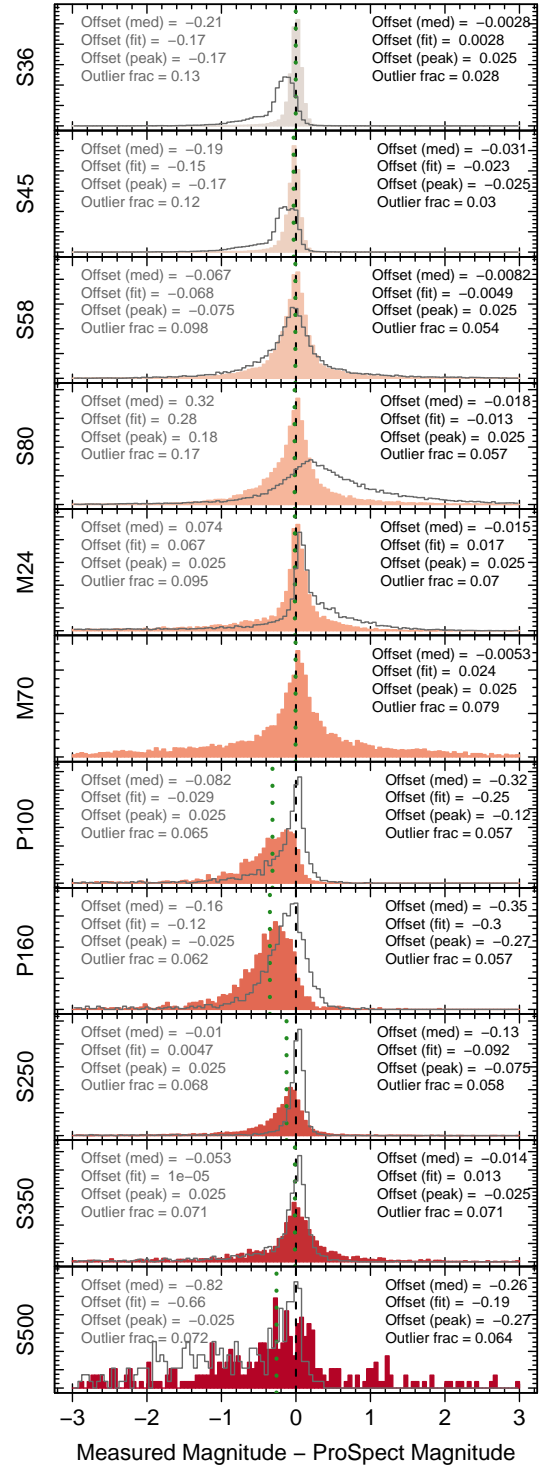


Figure 15. The same as Figure 14 but for the MIR-FIR (S36 - S500) bands.

comparisons, Figure 16 displays the interquartile range and outlier fraction for all colours, where a smaller value in each of these figures is desirable. Our new ProFOUND photometry does better (or comparable) to both existing datasets in all colours at FUV-160 μ m wavelengths. We do see a significantly larger outlier fractions in our FIR SPIRE measurements, which are consistent with the ProSPECT residual distributions shown in Figure 15, where the COSMOS2015

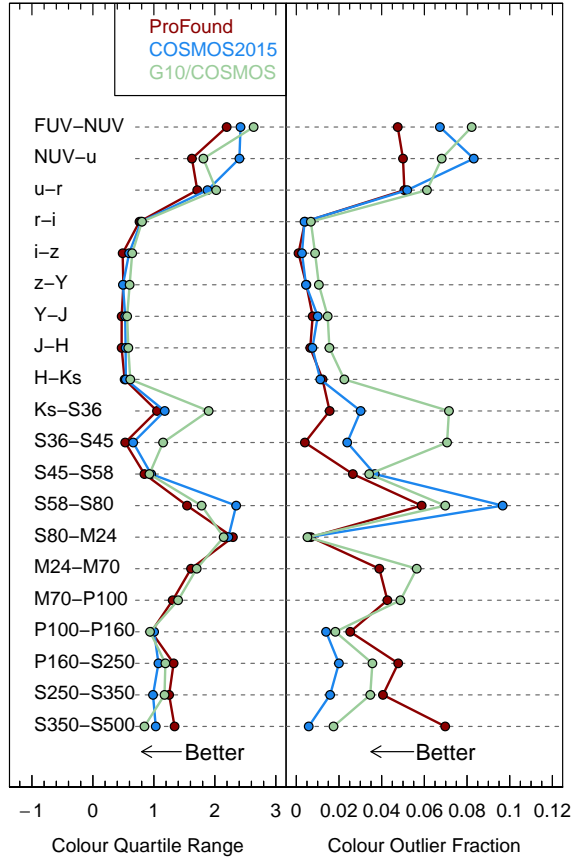


Figure 16. Comparison of colour histograms in adjacent filters for a matched sample of D10 ProFOUND, COSMOS2015 and G10/COSMOS galaxies. The left panel displays the interquartile range and right panel the outlier fraction. A smaller value in each of these figures is desirable.

photometry displays a more peaked distribution in the FIR. We have explored this discrepancy in a number of ways, and have been unable to improve the tightness of the colour distributions in our SPIRE photometry. However, for the sake of consistency between both our multi-wavelength photometry and the approach used in GAMA, we opt to retain our method for deriving the FIR photometry. We also note that only a small fraction of the DEVILS spectroscopic sample ($\sim 15\%$) have a detection in all of the SPIRE bands, and as such the DEVILS sample is unlikely to be significantly affected by these small differences in photometry.

7.4 Impact on derived physical properties

Following on from the above residuals and colour comparisons, it is also beneficial to assess how our new photometry catalogue impacts the derived properties of galaxies, when removing any other differences in the method for measuring these properties (*i.e.* how does the photometry alone change our galaxies physical properties and hence scientific conclusions). To do this we compare the SED-derived properties of a subsample of galaxies using the same method, but differing photometric measurements.

While we leave a full analysis of the DEVILS ProSPECT stellar mass and SFR measurements to [Thorne et al. \(2020\)](#), Figure 17 shows

a comparison of the ProSPECT-derived stellar masses and sSFR produced using the analysis/sample outlined in Section 7.2 (*i.e.* for an identical fitting procedure with ProSPECT but using both the COSMOS2015 photometry and our new ProFOUND photometry for an identical set of galaxies). We split the sample into three redshift bins between $0.2 < z < 0.8$ (see [Thorne et al. 2020](#), for a full description of this sample and redshifts) and display the difference between the resultant ProFOUND and COSMOS2015 stellar masses (top row), SFRs (middle row) and along the sSFR- M^* relation (bottom row). We find that derived stellar masses are consistent between the two samples, but with a systematic 0.1-0.2dex offset, but SFRs show a systematic bias to higher SFRs in ProFOUND in particular galaxy populations. This effect becomes more pronounced as we move to higher redshifts. This is most clearly apparent in the comparison of the sSFR- M^* relation where our ProFOUND and COSMOS2015 photometry produce a comparable relation at low redshift (median and scatter in sSFR are consistent at all stellar masses), but the samples begin to diverge significantly for $M^* < 10^{10} M_\odot$ galaxies at higher redshifts. Importantly this shows that *only* changing the photometric measurements for relatively bright galaxies, can have a significant impact on the measured evolution of the sSFR- M^* relation and associated conclusions. This just represents a single example where different photometric measurements can strongly impact derived scientific conclusions.

While it is still difficult to assess which sample would be deemed ‘correct’ through this analysis, we note that through the photometry measurements alone, a larger stellar mass and SFR (as is the case systematically from ProFOUND), suggests that one is measuring more true flux from the system, and therefore more robustly capturing the total emission from the galaxy. It is somewhat difficult to get the converse (systematically lower measurements) erroneously when only considering photometric measurement differences for a broad population of galaxies across a range of epochs. This, coupled with the analysis in Section 7.2, suggests that our new ProFOUND measurements are robustly capturing the total galaxy flux across a range of wavelengths, and thus can be used to measure galaxy properties (*i.e.* see [Thorne et al. 2020](#))

7.5 Astrometric Accuracy

Finally, to verify the astrometric accuracy of our catalogue, we perform a $2''$ match to $12 < g_{\text{GAIA}} < 18$ mag sources from the GAIA DR2 catalogues ([Gaia Collaboration et al. 2018](#); [Lindgren et al. 2018](#)). Figure 18 displays the R.A. and Dec offsets with the median offset marked as the blue cross. Circles indicate the UltraVISTA/VIDEO pixel size and typical seeing, showing that our final catalogues have sub-pixel astrometric accuracy in comparison to GAIA in D10. While we do see small (~ 1 pixel) offsets in D02/D03 we do not opt to correct for this astrometry mis-match. Instead we retain our catalogues with the astrometry derived from the DEVILS input catalogue photometry (*i.e.* derived from the UltraVISTA and VIDEO data directly). We note that the VIDEO data we use here has not been aligned with GAIA, but newer iterations and public releases will be.

8 DEEP NUMBER COUNTS

While our photometric catalogues are produced primarily to allow scientific analysis in a number of areas, they also provide some of the deepest photometric catalogues consistently measured over a broad wavelength range and over $> 1 \text{ deg}^2$ area scales. Here we use these

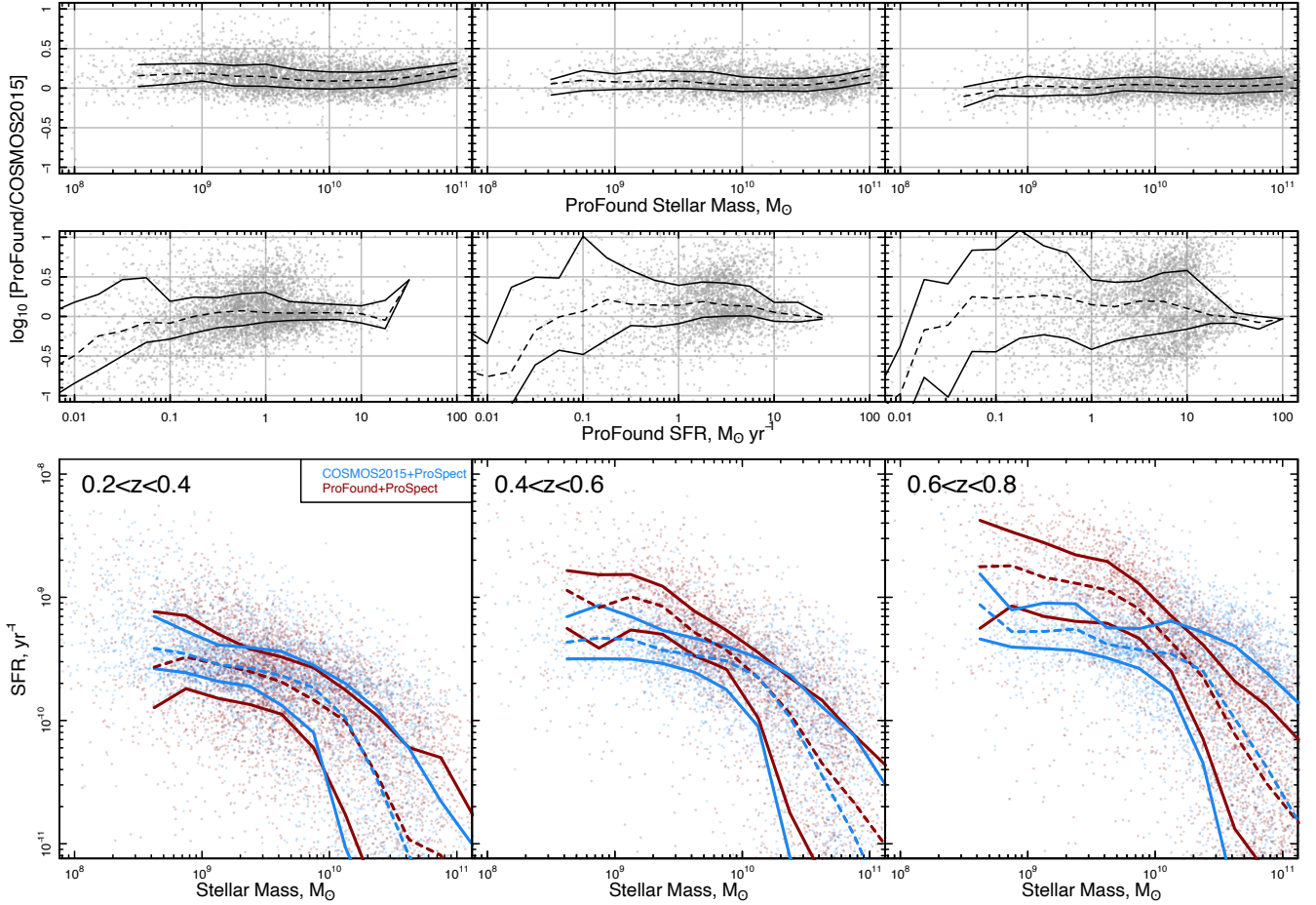


Figure 17. Comparison of the physical properties derived using ProSPECT for a common sample of galaxies but using both the COSMOS2015 photometry and our new ProFound photometry. We split the sample into three redshift bins between $0.2 < z < 0.8$. The top row displays the difference between stellar masses derived using the COSMOS2015 and ProFound photometry. Middle row show the same but for SFRs, while the bottom row shows the full sSFR- M^* relation for this sample. Stellar masses are consistent but with a 0.1-0.2 dex offset and the ProFound photometry produces systematically larger SFR which goes with sSFR. Combined this would lead to a distinctly different measurement of the evolution of the sSFR- M^* relation at $M^* < 10^{10} M_{\odot}$.

catalogues to produce deep galaxy number counts as an additional photometric validation, for the purposes of exploring the overall galaxy population in broader studies, and for tuning numerical simulations of the galaxy distribution. These number counts have recently been used in Koushan et al. (2021) to measure the Extragalactic Background Light (EBL) from the UV-MIR. Hence, we do not go into detail regarding the scientific implications of these distributions, but simply produce them and make available to the wider community.

Figures 19, 20, 21 and 22 display the number of galaxies in our unmasked regions per unit sky area (left column). We take all sources identified as galaxies using our selections described in Section 5.5.1, and bin in 0.5 mag ranges in each band and DEVILS field independently. Here we include both our NIR-selected catalogues and, in the FIR, include the ‘extra sources’ identified using ProFound (described in Section 6). We display the number counts for each DEVILS region independently as small gold, red and green circles and the combined counts for the full DEVILS sample as the larger blue circles. Error bars are derived from the Poisson error combined linearly with cosmic variance errors, estimated using the method outlined in Driver & Robotham (2010). In most cases, these error bars

are smaller than the data points. For comparison, we also display the compendium of photometric data from Driver et al. (2016a), and find remarkable agreement in the UV-MIR but now with smaller errors (the Driver et al. points essentially use just the COSMOS region at these depths and thus have larger Poisson and cosmic variance errors).

On these figures we also display the nominal quoted depth of the input imaging as the dashed vertical black lines (also given in Table 1), and the measured depth to galaxies in each field individually and for the full sample as the vertical coloured lines. These values are calculated as the point where each of the number count distributions turn over. These limits are displayed in the right column of these Figures and also in Table 1.

In order to highlight the small differences between each DEVILS region (and the literature values), in the right column of Figures 19, 20, 21 and 22 we also show these number counts with a 10^{th} order spline fit removed. The spline is fit to combined counts for the full DEVILS sample (blue circles) at magnitudes below the combined counts depth (vertical blue dashed lines). At fainter magnitudes we use the literature values from Driver et al. (2016a). We note that the

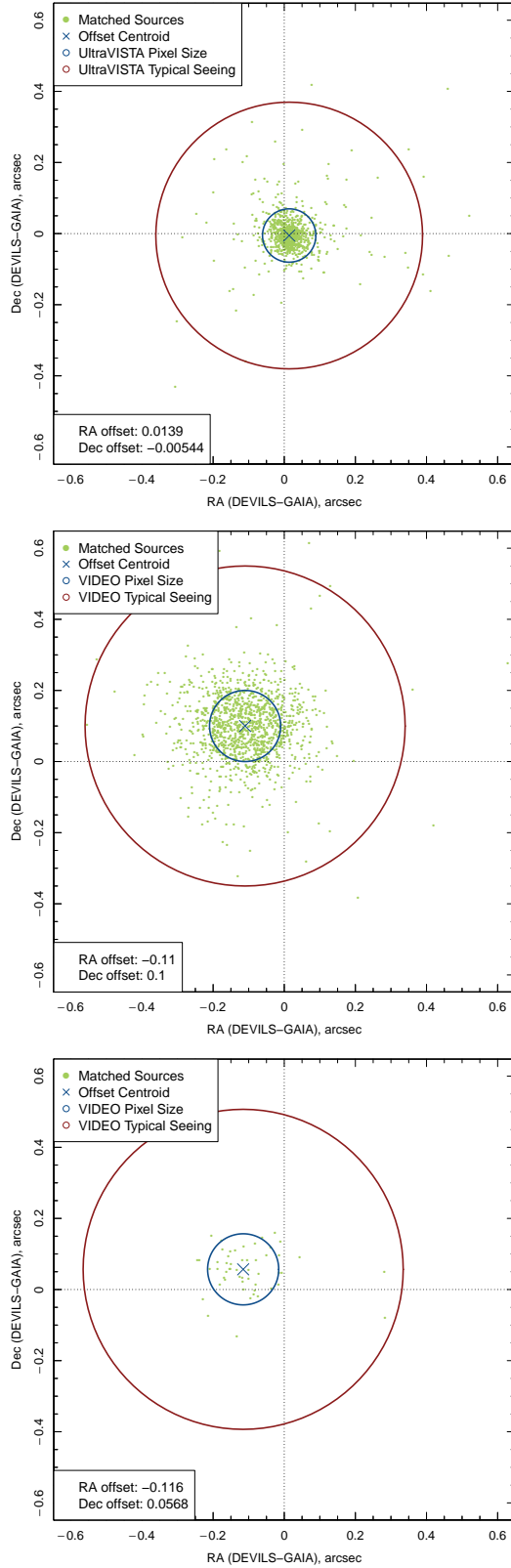


Figure 18. Astrometric accuracy of new catalogues against GAIA DR2 in each of the DEVILS regions (Top= D10, Middle=D02, Bottom=D03). The offsets in D02/D03 are driven by offsets in the VIDEO data astrometry.

choice of 10 degrees of freedom is largely arbitrary, but that changing this value does not significantly change our results.

We note that our deep number counts are measured consistently across all bands, with only small differences between fields at faint magnitudes. These counts extend to faint magnitudes over a large area $\sim 6 \text{ deg}^2$, making them the state-of-the-art in using galaxy number counts to explore the Universal distribution of flux at a given wavelength (Koushan et al. 2021). We therefore provide these for use in the larger community in a tabulated form in Table 5.

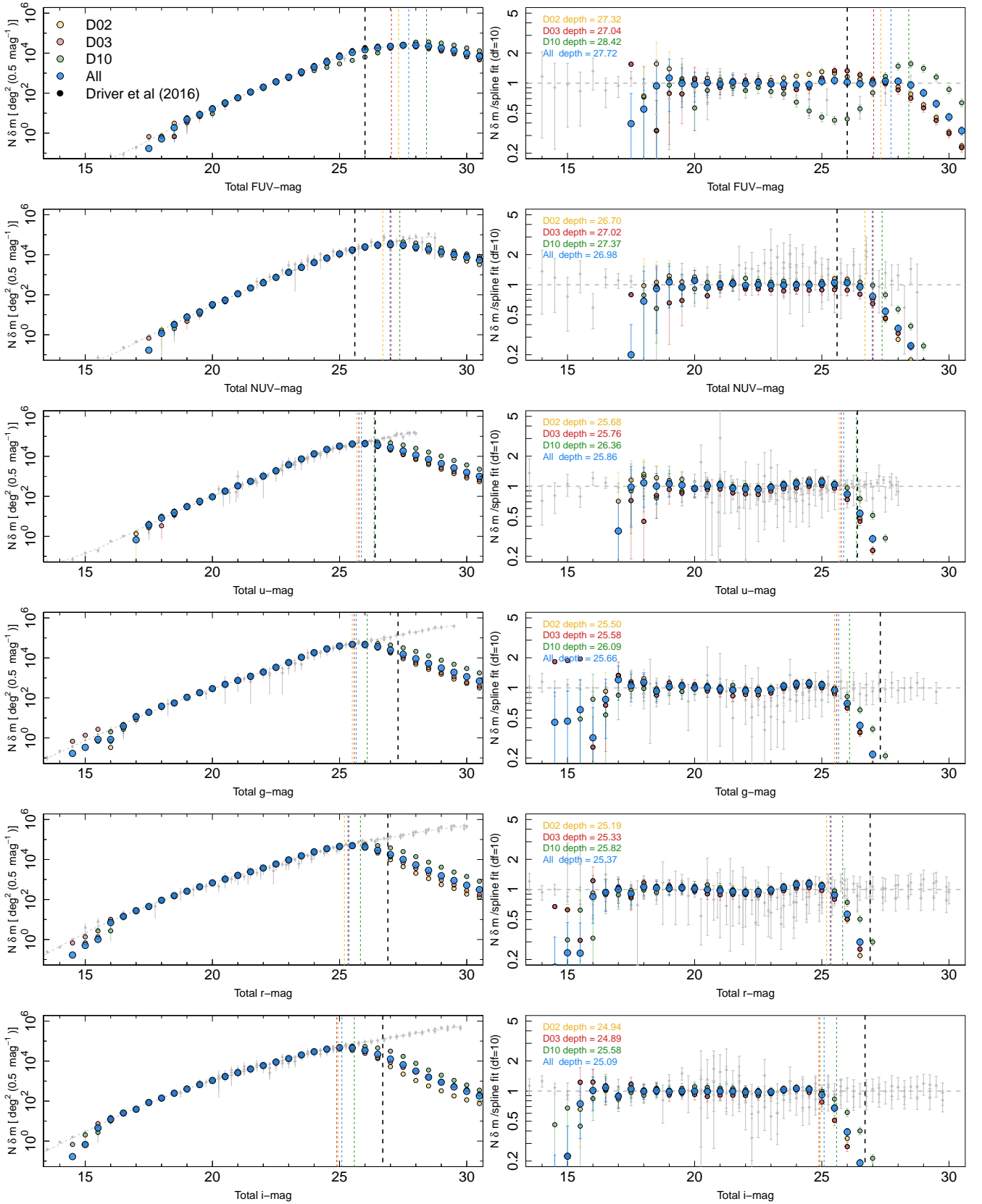


Figure 19. Deep galaxy number counts. We show each field individually for D02 (gold), D03 (red) and D10 (green), and for the full DEVILS sample (blue). Error bars (for Poisson+cosmic variance errors) are plotted, but in most cases are smaller than the data point. We also show the compendium of data from [Driver et al. \(2016a\)](#) as faint grey points. The left panel displays the number counts directly, while the right panel shows the number counts with a spline fit to the data removed (grey dashed line, see Section 8 for details). Also shown are the nominal survey quoted depth (black vertical dashed) and measured galaxy completeness depth for each individual field and the full sample (dashed vertical coloured lines). These depths are also noted in the left panel legend and Table 1.

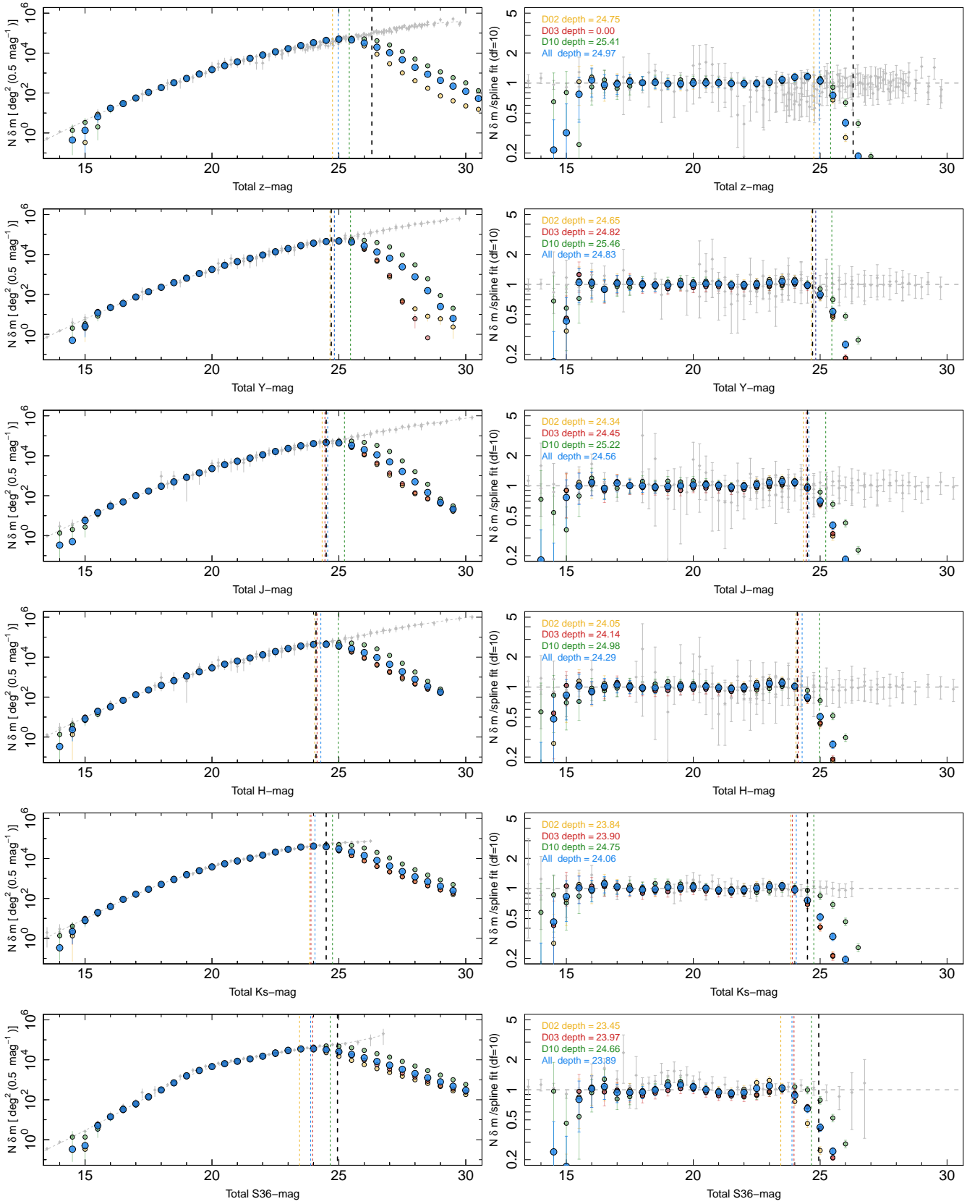


Figure 20. Figure 19 continued.

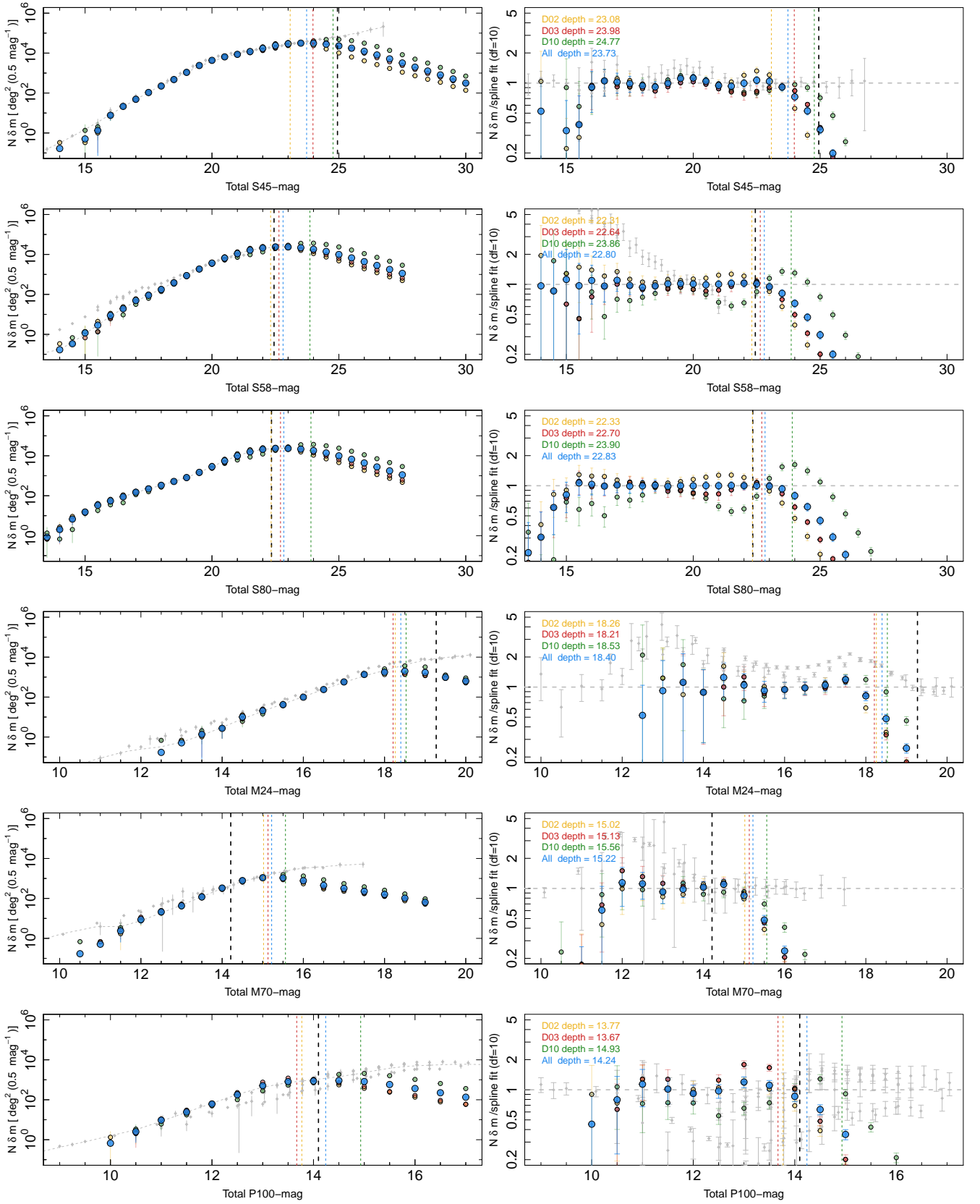


Figure 21. Figure 19 continued.

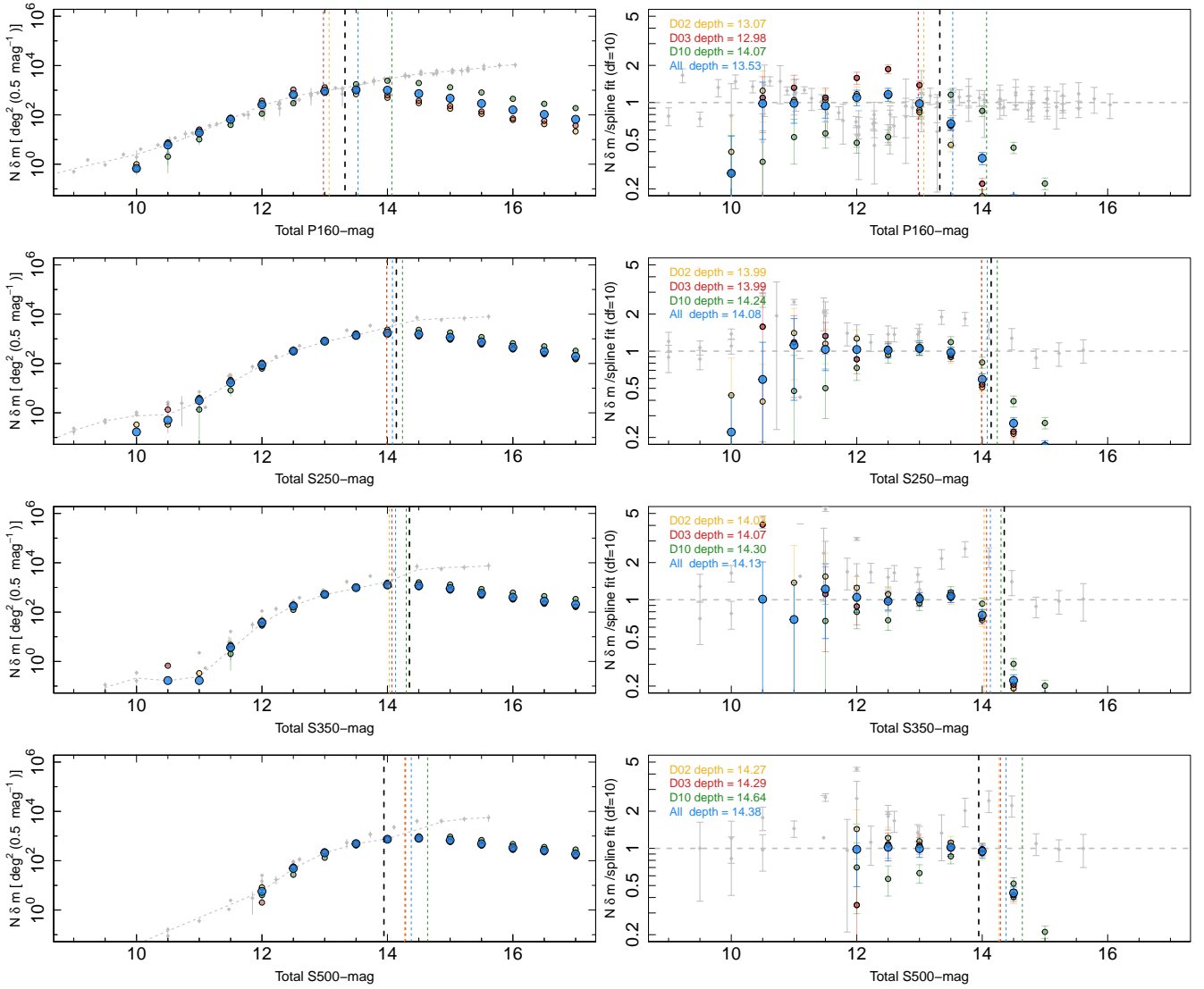


Figure 22. Figure 19 continued.

9 SUMMARY

We have derived a new photometric catalogue for the DEVILS regions for use in multiple scientific projects within the DEVILS team, which will then be provided to the wider community. Photometry is derived from the up-to-date imaging in these regions using the new ProFOUND source detection and photometry code, which is designed to overcome a number of known issues present in previous photometry. We perform a number of detailed checks and manual fixing of the ProFOUND segmentation maps to improve the validity of our photometric measurements and then drive new source photometry measurements from the UV-FIR. We apply a masking, artefact flagging and star/galaxy separation process to identify true extragalactic sources. We then undertake a series of comparisons to existing photometry in the D10 (COSMOS) region to highlight the validity of our catalogues and their use for scientific projects within DEVILS and the wider community. We also use these tests to suggest that our photometry is comparable or better than existing photometry in these regions. We note that these updates to the photometry can have a strong impact on derived galaxy evolution properties (such as the

evolution of the sSFR-M* relation). Finally, we use our catalogues to derive deep number counts in all photometric bands analysed in this work, which are measured consistently from the FUV to 500 μm , show consistency between individual fields and provide state-of-the-art galaxy number counts to faint magnitudes for the astronomical community.

ACKNOWLEDGEMENTS

LJMD, ASGR and LC acknowledge support from the *Australian Research Councils* Future Fellowship scheme (FT200100055, FT200100375 and FT180100066, respectively). JET is supported by the Australian Government Research Training Program (RTP) Scholarship. SB and SPD acknowledge support from the *Australian Research Councils* Discovery Project scheme (DP180103740). MS has been supported by the European Union's Horizon 2020 Research and Innovation programme under the Maria Skłodowska-Curie grant agreement (No. 754510), the Polish National Science Centre (UMO-2016/23/N/ST9/02963), and the Spanish Ministry of

Table 5. Tabulated number densities of sources in each photometric band. Magnitude is the centre of a $\Delta 0.5$ mag bin. All other values are $N(m)$, $0.5 \text{ mag}^{-1} \text{ deg}^{-2}$. These are also made available in a machine-readable form as online data products associated with this paper.

Mag.	FUV	NUV	u	g	r	i	z	Y	J	H
10.0	-	-	-	-	-	-	-	-	-	-
10.5	-	-	-	-	-	-	-	-	-	-
11.0	-	-	-	-	-	-	-	-	-	-
11.5	-	-	-	-	-	-	-	-	-	-
12.0	-	-	-	-	-	-	-	-	-	-
12.5	-	-	-	-	-	-	-	-	-	-
13.0	-	-	-	-	-	-	-	-	-	-
13.5	-	-	-	-	-	-	-	-	-	-
14.0	-	-	-	-	-	-	-	-	0.3±0.6	0.3±0.6
14.5	-	-	-	0.2±0.4	0.2±0.4	0.2±0.4	0.4±0.7	0.5±0.7	0.5±0.8	2.3±1.7
15.0	-	-	-	0.3±0.6	0.5±0.8	0.7±0.9	1.3±1.3	2.5±1.8	5.7±2.9	8.1±3.5
15.5	-	-	-	0.8±1.0	1.0±1.1	4.5±2.5	6.5±3.1	11.7±4.4	14.4±5.0	19.3±6.0
16.0	-	-	-	0.8±1.0	7.0±3.2	12.2±4.5	17.4±5.6	21.9±6.5	30.0±7.9	32.6±8.4
16.5	-	-	-	3.9±2.3	14.3±4.9	25.3±7.1	29.7±7.9	35.2±8.8	49.0±11.0	68.8±13.9
17.0	-	-	0.7±0.9	11.6±4.3	27.5±7.5	39.1±9.4	56.2±12.1	73.9±14.6	101±18	131±22
17.5	0.2±0.4	0.2±0.4	3.7±2.2	19.1±5.9	44.6±10.3	84.4±16.1	109±19	135±23	171±27	227±34
18.0	0.5±0.8	1.2±1.2	8.2±3.5	38.2±9.3	91.4±17.0	141±23	188±29	227±34	297±41	386±51
18.5	1.9±1.5	3.2±2.1	15.1±5.1	55.7±12.0	155±25	247±36	328±45	386±51	494±62	662±80
19.0	4.8±2.6	7.6±3.4	30.7±8.0	107±19	258±37	403±53	539±67	652±79	837±97	1137±126
19.5	8.6±3.6	13.6±4.8	55.7±12.0	183±28	430±56	668±80	898±103	1109±124	1397±151	1851±194
20.0	16.3±5.4	32.0±8.3	94.3±17.4	291±41	678±81	1071±120	1479±159	1776±187	2283±234	2903±291
20.5	32.5±8.4	53.6±11.7	182±28	476±61	1047±118	1690±179	2358±241	2848±286	3588±353	4437±428
21.0	58.5±12.4	111±20	334±46	751±89	1603±171	2643±267	3643±358	4364±422	5373±512	6371±599
21.5	113±20	217±32	563±70	1202±133	2439±248	4034±393	5455±519	6414±603	7660±712	9044±833
22.0	199±30	393±52	1023±115	1965±205	3739±366	5989±566	8003±742	9370±861	11227±1022	13116±1184
22.5	370±49	737±87	1899±198	3372±333	5944±562	8975±827	11559±1050	13572±1224	16399±1466	19021±1689
23.0	635±77	1317±144	3774±369	5939±561	9542±876	13336±1203	16732±1494	19713±1748	23484±2069	26909±2359
23.5	1130±126	2335±239	7383±688	10798±985	15371±1378	20295±1798	23943±2108	27671±2423	31971±2787	35937±3121
24.0	2002±208	4064±395	13391±1208	18361±1633	24211±2130	29416±2571	33312±2900	36667±3182	40744±3525	43078±3721
24.5	3598±353	6808±638	22224±1962	28471±2491	34965±3039	39707±3438	43335±3743	44337±3827	46237±3987	43808±3783
25.0	6690±627	11025±1004	32556±2836	39336±3407	45305±3908	47169±4065	50110±4311	47111±4060	44187±3814	36890±3201
25.5	10846±989	17263±1539	41211±3565	47325±4078	49256±4240	45640±3936	46263±3989	42220±3649	33304±2899	26126±2293
26.0	14840±1332	24679±2170	43026±3717	45773±3948	41809±3615	34209±2975	32160±2803	26500±2324	20150±1786	16906±1509
26.5	18398±1636	30594±2670	36589±3176	36117±3136	28939±2531	21662±1914	19592±1738	13287±1199	11125±1013	9485±871
27.0	21876±1932	32558±2836	27218±2385	24624±2165	17667±1574	12604±1140	10409±951	6466±608	4966±476	4360±422
27.5	24730±2174	30018±2622	18389±1636	15211±1364	10103±925	6558±616	4650±448	2395±244	1638±174	1877±196

Mag.	Ks	S36	S45	S58	S80	M24	M70	P100	P160	S250	S350	S500
10.0	-	-	-	-	-	-	-	0.7±0.9	0.7±0.9	0.2±0.4	-	-
10.5	-	-	-	-	-	-	-	0.2±0.4	2.5±1.8	6.0±2.9	0.5±0.7	0.2±0.4
11.0	-	-	-	-	-	-	-	0.5±0.8	9.5±3.9	19.1±5.9	3.2±2.0	0.2±0.4
11.5	-	-	-	-	-	-	-	2.4±1.7	24.1±6.9	65.6±13.5	16.7±5.5	3.7±2.2
12.0	-	-	-	-	-	-	-	8.7±3.7	61.6±12.9	261±37	87.7±16.5	37.3±9.2
12.5	-	-	-	-	0.2±0.4	0.2±0.4	21.1±6.3	179±28	661±80	319±44	177±28	48.9±11.0
13.0	-	-	-	-	0.2±0.4	0.5±0.8	42.5±10.0	508±64	921±105	801±94	521±65	208±31
13.5	-	-	-	-	0.8±1.0	1.4±1.3	119±21	808±94	1026±116	1371±149	979±111	492±62
14.0	0.3±0.6	-	0.2±0.4	0.2±0.4	2.0±1.6	2.7±1.9	330±45	871±101	1004±114	1708±181	1265±139	743±88
14.5	2.2±1.7	0.3±0.6	-	0.3±0.6	6.8±3.2	10.0±4.0	782±92	912±105	729±86	1533±164	1183±131	818±95
15.0	7.9±3.5	0.5±0.7	0.5±0.7	1.2±1.2	15.2±5.1	20.6±6.2	1084±122	819±95	472±60	1157±128	899±103	673±81
15.5	19.8±6.1	5.0±2.7	1.3±1.3	2.9±1.9	33.6±8.5	41.8±9.9	1071±120	581±71	290±41	747±88	577±71	485±62
16.0	39.0±9.4	14.1±4.9	7.7±3.4	8.8±3.7	54.8±11.9	98.6±18.0	767±90	367±49	160±26	450±58	399±53	334±45
16.5	89.7±16.8	32.6±8.4	21.4±6.4	19.1±5.9	88.4±16.6	239±35	450±58	224±33	105±19	308±43	277±39	262±38
17.0	163±26	62.8±13.0	48.7±11.0	49.2±11.0	149±24	573±71	318±44	135±23	66.5±13.6	195±30	207±31	188±29
17.5	288±40	139±23	106±19	90.1±16.8	221±33	1355±148	227±34	80.5±15.5	46.0±10.5	125±21	140±23	140±23
18.0	505±64	310±43	224±33	175±28	333±45	1769±187	160±26	45.2±10.4	25.6±7.2	78.5±15.3	84.2±16.0	90.9±17.0
18.5	885±102	702±84	474±60	382±51	519±65	1970±205	103±19	28.1±7.6	15.9±5.3	39.0±9.4	49.2±11.0	53.1±11.6
19.0	1544±165	1578±168	1084±121	872±101	812±95	1704±180	64.3±13.3	12.6±4.6	8.0±3.5	28.5±7.7	35.7±8.9	37.0±9.1
19.5	2442±249	2937±294	2399±245	1857±195	1475±159	978±111	34.2±8.6	12.4±4.5	5.9±2.9	17.9±5.7	22.1±6.5	20.8±6.2
20.0	3792±371	4594±443	4333±419	3670±360	2841±285	632±77	23.0±6.7	7.0±3.2	2.7±1.9	12.9±4.6	14.7±5.0	14.1±4.9
20.5	5435±518	6415±603	6479±609	6549±615	5539±526	409±54	12.8±4.6	5.0±2.7	2.3±1.7	9.2±3.8	10.0±4.0	13.2±4.7
21.0	7471±697	8449±781	8654±799	10931±996	9961±912	244±36	9.7±3.9	1.7±1.4	0.7±0.9	9.5±3.9	8.0±3.5	10.5±4.1
21.5	10410±953	11104±1011	11900±1080	16357±1462	15866±1420	156±25	7.0±3.2	1.5±1.4	1.3±1.3	8.7±3.7	9.7±3.9	10.0±4.0
22.0	14741±1326	15157±1359	17134±1528	21138±1870	20990±1857	97.1±17.8	9.2±3.8	1.7±1.4	0.7±0.9	10.0±4.0	16.2±5.4	10.0±4.0
22.5	20908±1853	21886±1933	23843±2099	23849±2100	23591±2078	57.1±12.2	10.5±4.1	1.2±1.2	1.0±1.1	12.1±4.5	17.6±5.6	13.2±4.7
23.0	28899±2531	29775±2601	29204±2553	23801±2096	23398±2061	29.9±7.9	9.0±3.7	0.7±0.9	1.3±1.3	9.4±3.8	18.8±5.9	19.1±5.9
23.5	37206±3233	34960±3039	31488±2746	21688±1916	21586±1908	21.8±6.4	9.4±3.8	0.3±0.6	0.5±0.7	8.2±3.5	17.4±5.6	19.6±6.0
24.0	41654±3608	35913±3119	31040±2708	18234±1622	18162±1616	12.4±4.5	8.0±3.5	0.3±0.6	0.7±0.9	9.9±3.9	13.2±4.7	24.3±6.9
24.5	38743±3362	32089±2797	27997±2451	14033±1263	13840±1247	7.5±3.3	12.4±4.5	-	0.5±0.7	10.2±4.0	10.7±4.1	20.3±6.2
25.0	30352±2654	25586±2247	23053±2032	9904±907	9915±908	4.9±2.6	10.4±4.1	-	0.8±1.0	7.7±3.4	14.7±5.0	23.1±6.7
25.5	21584±1911	18657±1658	17589±1567	6704±629	6675±626	1.0±1.1	10.9±4.2	-	0.7±0.9	8.0±3.5	15.7±5.3	15.4±5.2
26.0	13944±1257	12613±1141	12319±1116	4359±422	4380±423	2.6±1.8	10.7±4.1	0.2±0.4	1.2±1.2	6.7±3.1	11.2±4.3	20.6±6.2
26.5	7989±742	8253±764	8058±747	2813±282	2762±278	0.9±1.0	12.4±4.5	-	0.2±0.4	6.9±3.2	12.7±4.6	17.7±5.7
27.0	4208±409	5398±514	5139±491	1774±187	1763±186	0.9±1.0	11.9±4.4	-	0.3±0.6	6.5±3.1	12.9±4.6	17.6±5.6
27.5	2219±228	3350±331	3201±318	1129±126	1112±124	0.9±1.0	8.7±3.7	-	1.2±1.2	7.5±3.4	12.2±4.5	13.9±4.9

Table 6. DEVILS photometric catalogue columns available in DEVILS_PhotomCat_15_10_2020_v0.5. The *B* values are available for *FUV NUV ugrizYJHK_s S36 S45 S58 S80 MIPS24 MIPS70 P100 P160 S250 S350 S500* μ m bands.

Column Name	Unit	UCD	Description
UID	none	meta.id	UID based on field location, and source RAm _{ax} and DEC _{max}
NewSegID	none	meta.id	Segment ID derived from segmentation maps - unique over full field
field	none	meta.id	DEVILS Field identifier (D02/D03/D10)
RAcen	deg	pos.eq.ra	Right ascension of the ProFound segment centre in the VISTA Y-band image
DECcen	deg	pos.eq.dec	Declination of the ProFound segment centre in the VISTA Y-band image
RAmax	deg	pos.eq.ra	Right ascension of the brightest pixel in ProFound segment in the VISTA Y-band image
DECmax	deg	pos.eq.dec	Declinations of the brightest pixel in ProFound segment in the VISTA Y-band image
mask	none	meta.id	Mask flag to identify if segment falls in a masked region. 0=not masked, 1=masked
artefactFlag	none	meta.id	Artefact flag 0=Not artefact, >0=artefact
starFlag	none	meta.id	Star/galaxy classifier. 0=galaxy, 1=star
R50_Y	"	phys.angSize;em.IR.Y	The segment radius contain 50% of the VISTA Y-band flux
N100_Y	none	phys.area	Number of segment pixels in the VISTA Y-band
subFrame	none	meta.id	ProFound processing subFrame within the field that the segment is taken from
segIDFrame	none	meta.id	Segment ID within subFrame
xcenFrame	pixel	instr.pixel	x position of the segment centre within the subFrame in the VISTA Y-band
ycenFrame	pixel	instr.pixel	y position of the segment centre within the subFrame in the VISTA Y-band
xmaxFrame	pixel	instr.pixel	x position of the segment brightest pixel within the subFrame in the VISTA Y-band
ymaxFrame	pixel	instr.pixel	y position of the segment brightest pixel within the subFrame in the VISTA Y-band
EBV	none	phys.excitParam	Galactic Extinction coefficient applied - derived from Planck maps
flux_*B*	Jy	phot.flux.density;em.*B*	Total flux measured in *B*
flux_err_*B*	Jy	stat.error;phot.flux.density;em.*B*	Error on total flux measured in *B*
flux_*B*_c	Jy	phot.flux.density;em.*B*	Colour-optimised flux measured in *B*
flux_err_*B*_c	Jy	stat.error;phot.flux.density;em.*B*	Error on colour-optimised flux measured in *B*

Science and Innovation through the Juan de la Cierva-formacion programme (FJC2018-038792-I). MJJ acknowledges support from the UK Science and Technology Facilities Council [ST/S000488/1 and ST/N000919/1], the Oxford Hintze Centre for Astrophysical Surveys which is funded through generous support from the Hintze Family Charitable Foundation and the South African Radio Astronomy Observatory (SARAO), and ICRAR for financial support during a sabbatical visit. MBI is supported by the Polish National Science Center through grants no. 2020/38/E/ST9/00395, 2018/30/E/ST9/00698 and 2018/31/G/ST9/03388, and by the Polish Ministry of Science and Higher Education through grant DIR/WK/2018/12. MV acknowledges support from the Italian Ministry of Foreign Affairs and International Cooperation (MAECI Grant Number ZA18GR02) and the South African Department of Science and Innovation's National Research Foundation (DSI-NRF Grant Number 113121) as part of the ISARP RADIOSKY2020 Joint Research Scheme. NM acknowledges support from the Bundesministerium für Bildung und Forschung (BMBF) award 05A20WM4. MBr acknowledges the support of the University of Western Australia through a Scholarship for International Research Fees and Ad Hoc Postgraduate Scholarship. DEVILS is an Australian project based around a spectroscopic campaign using the Anglo-Australian Telescope. DEVILS is part funded via Discovery Programs by the *Australian Research Council* and the participating institutions. The DEVILS website is <https://devilsurvey.org>. The DEVILS data is hosted and provided by AAO Data Central (datacentral.org.au).

10 DATA AVAILABILITY

The photometry catalogues and associated meta data derived in this work are currently made available to the DEVILS team for internal use via a Data Management Unit (DMU) describing the data origin, and providing all photometric measurements and other useful parameters provided by ProFound. Each DMU is both version and date

stamped for ease of use and to keep track of updates. The catalogue used in this paper is DEVILS_PhotomCat_15_10_2020_v0.5 with columns described in Table 6. The data are currently available for proprietary data projects within DEVILS. However, once these data have been used for core DEVILS science projects, it will be made available to the wider community via AAO data central¹⁰.

REFERENCES

- Abazajian K. N., Adelman-McCarthy J. K., Agüeros M. A., Allam S. S., Allende Prieto C., An D., Anderson K. S. J., et al., 2009, *ApJS*, 182, 543. doi:10.1088/0067-0049/182/2/543
- Adams N. J., Bowler R. A. A., Jarvis M. J., Häußler B., McLure R. J., Bunker A., Dunlop J. S., et al., 2020, *MNRAS*, 494, 1771. doi:10.1093/mnras/staa687
- Aihara H., et al., 2018, *PASJ*, 70, S4
- Aihara H., et al., 2018, *PASJ*, 70, S8
- Aihara H., et al., 2019, *PASJ*, tmp, 106
- Alpaslan M., Robotham A. S. G., Obreschkow D., Penny S., Driver S., Norberg P., Brough S., et al., 2014, *MNRAS*, 440, L106. doi:10.1093/mnrasl/slu019
- Alpaslan M., Grootes M., Marcum P. M., Popescu C., Tuffs R., Bland-Hawthorn J., Brough S., et al., 2016, *MNRAS*, 457, 2287. doi:10.1093/mnras/stw134
- Andrews S. K., Driver S. P., Davies L. J. M., Kafle P. R., Robotham A. S. G., Wright A. H., 2017, *MNRAS*, 464, 1569
- Baldry I. K., et al., 2010, *MNRAS*, 404, 86
- Baldry I. K., et al., 2012, *MNRAS*, 421, 621
- Baldry I. K., Liske J., Brown M. J. I., Robotham A. S. G., Driver S. P., Dunne L., Alpaslan M., et al., 2018, *MNRAS*, 474, 3875. doi:10.1093/mnras/stx3042
- Bellstedt S., Driver S. P., Robotham A. S. G., Davies L. J. M., Bogue C. R. J.,

¹⁰ <https://datacentral.org.au/>

- Cook R. H. W., Hashemizadeh A., et al., 2020, *MNRAS*, 496, 3235. doi:10.1093/mnras/staa1466
- Bellstedt S., Robotham A. S. G., Driver S. P., Thorne J. E., Davies L. J. M., Holwerda B. W., Hopkins A. M., et al., 2021, arXiv, arXiv:2102.11514
- Bertin E., Arnouts S., 1996, *A&AS*, 117, 393
- Bertin E., Mellier Y., Radovich M., Missonnier G., Didelon P., Morin B., 2002, *ASPC*, 228, ASPC.281
- Blake C., Baldry I. K., Bland-Hawthorn J., Christodoulou L., Colless M., Conselice C., Driver S. P., et al., 2013, *MNRAS*, 436, 3089. doi:10.1093/mnras/stt1791
- Blanton M. R., Eisenstein D., Hogg D. W., Schlegel D. J., Brinkmann J., 2005, *ApJ*, 629, 143. doi:10.1086/422897
- Brinchmann J., Charlot S., White S. D. M., Tremonti C., Kauffmann G., Heckman T., Brinkmann J., 2004, *MNRAS*, 351, 1151. doi:10.1111/j.1365-2966.2004.07881.x
- Capak P., et al., 2007, *ApJS*, 172, 99
- Cooper, M. C., Griffith, R. L., Newman, J. A., et al. 2012, *MNRAS*, 419, 3018
- Davies L. J. M., et al., 2015, *MNRAS*, 447, 1014
- Davies L. J. M., et al., 2015, *MNRAS*, 452, 616
- Davies L. J. M., et al., 2016, *MNRAS*, 455, 4013
- Davies L. J. M., et al., 2016, *MNRAS*, 461, 458
- Davies L. J. M., Huynh M. T., Hopkins A. M., Seymour N., Driver S. P., Robotham A. G. R., Baldry I. K., et al., 2017, *MNRAS*, 466, 2312. doi:10.1093/mnras/stw3080
- Davies L. J. M., et al., 2018, *MNRAS*, 480, 768
- Davies L. J. M., Lagos C. del P., Katsianis A., Robotham A. S. G., Cortese L., Driver S. P., Bremer M. N., et al., 2019, *MNRAS*, 483, 1881. doi:10.1093/mnras/sty2957
- Davies L. J. M., Robotham A. S. G., Lagos C. del P., Driver S. P., Stevens A. R. H., Bahé Y. M., Alpaslan M., et al., 2019, *MNRAS*, 483, 5444. doi:10.1093/mnras/sty3393
- Driver S. P., Robotham A. S. G., 2010, *MNRAS*, 407, 2131
- Driver S. P., et al., 2011, *MNRAS*, 413, 971
- Driver S. P., et al., 2016, *ApJ*, 827, 108
- Driver S. P., et al., 2018, *MNRAS*, 475, 2891
- Ellison S. L., Patton D. R., Simard L., McConnachie A. W., 2008, *AJ*, 135, 1877. doi:10.1088/0004-6256/135/5/1877
- Frayer D. T., Sanders D. B., Surace J. A., Aussel H., Salvato M., Le Floch E., Huynh M. T., et al., 2009, *AJ*, 138, 1261. doi:10.1088/0004-6256/138/5/1261
- Gaia Collaboration, Brown A. G. A., Vallenari A., Prusti T., de Bruijne J. H. J., Babusiaux C., Bailer-Jones C. A. L., et al., 2018, *A&A*, 616, A1. doi:10.1051/0004-6361/201833051
- Gordon K. D., Engelbracht C. W., Rieke G. H., Misselt K. A., Smith J.-D. T., Kennicutt R. C., 2008, *ApJ*, 682, 336. doi:10.1086/589567
- Guzzo L., Scodreggio M., Garilli B., Granett B. R., Fritz A., Abbas U., Adami C., et al., 2014, *A&A*, 566, A108. doi:10.1051/0004-6361/201321489
- Hashemizadeh A., Driver S. P., Davies L. J. M., Robotham A. S. G., Bellstedt S., Windhorst R. A., Bremer M., et al., 2021, arXiv, arXiv:2102.13377
- Hopkins A. M., Driver S. P., Brough S., Owers M. S., Bauer A. E., Guawardhana M. L. P., Cluver M. E., et al., 2013, *MNRAS*, 430, 2047. doi:10.1093/mnras/stt030
- Hurley P. D., et al., 2017, *MNRAS*, 464, 885
- Jarvis M. J., et al., 2013, *MNRAS*, 428, 1281
- Kauffmann G., Heckman T. M., White S. D. M., Charlot S., Tremonti C., Brinchmann J., Bruzual G., et al., 2003, *MNRAS*, 341, 33. doi:10.1046/j.1365-8711.2003.06291.x
- Koushan S., Driver S. P., Bellstedt S., Davies L. J., Robotham A. S. G., Lagos C. del P., Hashemizadeh A., et al., 2021, *MNRAS*.tmp. doi:10.1093/mnras/stab540
- Laigle C., et al., 2016, *ApJS*, 224, 24
- Lange R., et al., 2015, *MNRAS*, 447, 2603
- Lara-López M. A., Hopkins A. M., López-Sánchez A. R., Brough S., Guawardhana M. L. P., Colless M., Robotham A. S. G., et al., 2013, *MNRAS*, 434, 451. doi:10.1093/mnras/stt1031
- Levenson L., et al., 2010, *MNRAS*, 409, 83
- Lilly S. J., et al., 2007, *ApJS*, 172, 70
- Lin L., et al., 2016, *ApJ*, 817, 97
- Lindgren L., Hernández J., Bombrun A., Klioner S., Bastian U., Ramos-Lerate M., de Torres A., et al., 2018, *A&A*, 616, A2. doi:10.1051/0004-6361/201832727
- Liske J., et al., 2015, *MNRAS*, 452, 2087
- Lonsdale C. J., et al., 2003, *PASP*, 115, 897
- Lutz D., et al., 2011, *A&A*, 532, A90
- Mauduit J.-C., et al., 2012, *PASP*, 124, 714
- McCracken H. J., et al., 2012, *A&A*, 544, A156
- Moffett A. J., et al., 2016, *MNRAS*, 462, 4336
- Newman, J. A., Cooper, M. C., Davis, M., et al. 2013, *ApJS*, 208, 5
- Oliver S. J., et al., 2012, *MNRAS*, 424, 1614
- Panther B., Heavens A. F., Jimenez R., 2004, *MNRAS*, 355, 764
- Patton D. R., Ellison S. L., Simard L., McConnachie A. W., Mendel J. T., 2011, *MNRAS*, 412, 591. doi:10.1111/j.1365-2966.2010.17932.x
- Patton D. R., Torrey P., Ellison S. L., Mendel J. T., Scudder J. M., 2013, *MNRAS*, 433, L59. doi:10.1093/mnras/slt058
- Peng Y.-j., et al., 2010, *ApJ*, 721, 193
- Planck Collaboration, et al., 2016, *A&A*, 594, A1
- Robotham A. S. G., et al., 2011, *MNRAS*, 416, 2640
- Robotham A. S. G., Driver S. P., Sansom A. E., Baldry I. K., Bauer A. E., Bland-Hawthorn J., et al., 2013, *MNRAS*, 431, 167. doi:10.1093/mnras/stt156
- Robotham A. S. G., et al., 2014, *MNRAS*, 444, 3986
- Robotham A. S. G., Davies L. J. M., Driver S. P., Koushan S., Taranu D. S., Casura S., Liske J., 2018, arXiv, arXiv:1802.00937
- Robotham A. S. G., Bellstedt S., Lagos C. del P., Thorne J. E., Davies L. J., Driver S. P., Bravo M., 2020, *MNRAS*, 495, 905. doi:10.1093/mnras/staa1116
- Sanders D. B., et al., 2007, *ApJS*, 172, 86
- Schlafly E. F., Finkbeiner D. P., 2011, *ApJ*, 737, 103. doi:10.1088/0004-637X/737/2/103
- Scodreggio M., Guzzo L., Garilli B., Granett B. R., Bolzonella M., de la Torre S., Abbas U., et al., 2018, *A&A*, 609, A84. doi:10.1051/0004-6361/201630114
- Scoville N., et al., 2007, *ApJS*, 172, 1
- Taylor E. N., et al., 2015, *MNRAS*, 446, 2144
- Tegmark M., Blanton M. R., Strauss M. A., Hoyle F., Schlegel D., Scoccamarro R., Vogeley M. S., et al., 2004, *ApJ*, 606, 702. doi:10.1086/382125
- Thorne J. E., Robotham A. S. G., Davies L. J. M., Bellstedt S., Driver S. P., Bravo M., Bremer M. N., et al., 2020, arXiv, arXiv:2011.13605
- Tremonti C. A., Heckman T. M., Kauffmann G., Brinchmann J., Charlot S., White S. D. M., Seibert M., et al., 2004, *ApJ*, 613, 898. doi:10.1086/423264
- Vaccari M., et al., 2016, *heas.conf*, 26,
- Viero M. P., et al., 2013, *ApJ*, 779, 32
- Wright A. H., et al., 2016, *MNRAS*, 460, 765
- Wright A. H., et al., 2017, *MNRAS*, 470, 283
- Yang X., Mo H. J., van den Bosch F. C., Pasquali A., Li C., Barden M., 2007, *ApJ*, 671, 153
- York D. G., Adelman J., Anderson J. E., Anderson S. F., Annis J., Bahcall N. A., Bakken J. A., et al., 2000, *AJ*, 120, 1579. doi:10.1086/301513
- Zamojski M. A., et al., 2007, *ApJS*, 172, 468

This paper has been typeset from a $\mathrm{\LaTeX}$ file prepared by the author.